Effect of the scanning strategy and tribological conditions on the wear resistance of IN718 obtained by Laser Metal Deposition

Théo Zurcher, Gaëtan Bouvard, Jean-Christophe Abry, Eric Charkaluk, Vincent Fridrici

Effect of the scanning strategy and tribological conditions on the wear resistance of IN718 obtained by Laser Metal Deposition

Théo Zurcher[1,2,*], Gaëtan Bouvard[1], Jean-Christophe Abry[1], Eric Charkaluk[2], and Vincent Fridrici[1,**]

[1]Ecole Centrale de Lyon, Laboratoire de Tribologie et Dynamique des Systèmes, UMR CNRS 5513 ECL-ENTPE, Ecully, 69130, France
[2]Ecole Polytechnique, Laboratoire de Mécanique des Solides, UMR CNRS 7649, Palaiseau, 91120, France
*theo.zurcher@polytechnique.edu
**vincent.fridrici@ec-lyon.fr

Abstract

Since the advent of additive manufacturing processes, new ways of repairing damaged parts emerged. Among those, Laser Metal Deposition offers the possibility of restoration or functionalization of surface properties. In this work, we study the wear properties of an IN718 coating deposited by LMD. IN718 is deposited according to several scanning strategies. Samples are subjected to dry flat-on-flat reciprocating wear tests using the flat surface of a cylindrical pin as a counter body. Then, we investigate the impact of the scanning strategy, the normal load, and the number of cycles on wear. Finally, we compare the wear resistance of the LMD samples with the one of wrought IN718 to evaluate the competitiveness of the wear properties of the material obtained by LMD. Results show that the scanning strategy turns out to not change the wear resistance of the deposited sample despite the highly heterogeneous surface microstructure. As the chosen contact is a flat-on-flat contact, the large area covered by the pin does not perceive the local microstructural heterogeneities. It has been observed as well that the wear volume of the coating increases linearly as the normal load increases, with an evolution of the wear mechanisms. Although oxidized transfer layer is observed at lower load, the main wear mechanisms observed are abrasion and adhesion. Then, by studying the wear evolution with increasing testing time, it has been observed that after a certain amount of cycles, a protective oxide layer appears and prevents IN718 from wear. In similar tribological conditions, wrought IN718 has slightly better wear resistance than its LMD's homolog. This difference in wear between the materials obtained by two processes could certainly be explained by the high initial amount of dislocations in the LMD samples and the presence of detrimental phases in its microstructure, such as Laves phases. Nonetheless, this study highlights the good wear resistance of the IN718 samples obtained by LMD despite their non-optimized as-built properties.

Keywords: Additive manufacturing, wear, IN718, coating, scanning strategy

1. Introduction

Laser Metal Deposition (LMD) is an additive manufacturing (AM) technique belonging to the direct energy deposition (DED) process family. By the intermediate of a coaxial nozzle, metallic powder is projected underneath the focal point of a powerful laser. The laser creates a melt pool which is fed by the continuous powder stream. After solidification, it creates a small bead. A 3D part is built by juxtaposing beads to form a layer and piling up the layers. This process allows the manufacturing of geometrical complex parts but it also has other interesting features, including the possibility of adding functions to a pre-existing metallic part or restoring worn-out parts [1]. This article is focused on the wear behavior of IN718 deposited by LMD. The obtained results might be interesting for the use of LMD as a repairing process for worn parts.

The restoration of metallic parts is already possible through several different processes such as arc welding [2], thermal spray [3], etc… However, using the LMD technique gives the advantage of accurately repairing parts with complex geometric shapes. In the aerospace/aeronautic fields, turbine blades made up of nickel superalloy have been already repaired through this process [4]–[6]. Other studies focused their works on die repair by depositing harder alloys than the initial die material [7], [8]. Aditya et al. [9] tried to clad a Co-Ni secondary hardening steel in readiness for the repairing of components such as pinion housing shafts or gears. In our case, the alloy used for repairing is Inconel718 (IN718).

IN718 is a very well-known nickel-based precipitation-strengthening alloy. Its high amount of iron made him interesting economically but with a slightly lower corrosion resistance compared to other Inconel grades (such as IN625 for instance) in which the iron is replaced by other alloying elements such as Co, Ta, Mo etc. When conventionally manufactured, this alloy is mainly composed of an austenitic matrix γ in which the γ’ and γ“ coherent strengthening phases are precipitated after that a usual homogenization and double aging heat treatment is carried out. Because of its good mechanical properties and corrosion resistance at high temperatures (above 650°C), this alloy is one of the primary compounds of aerospace engine parts [10]. Therefore, because of its good properties and weldability, many articles cover the shaping of this material through the LMD process [11]–[13]. These articles focused on process parameter optimization, the resulting microstructure, and its mechanical properties. Generally, results in the literature highlighted the fact that the additive manufacturing process gives rise to differences in mechanical properties compared to parts produced by a conventional process [14]. However, only very few articles considered the tribological properties of IN718 deposited by LMD. More generally, the wear resistance of additive-manufactured parts is still a juvenile research topic.

Yang et al. worked on the wear behavior of the 316L stainless steel produced by Laser Powder Bed Fusion (LPBF) [15]. They brought to light an anisotropic wear behavior and showed that the typical cellular sub-microstructure of this alloy when manufactured by LPBF plays a crucial role in its wear properties. More recently, the same authors exposed the impact of the microstructural texture on its wear behavior. According to them, it would be possible to reduce the wear rate by tailoring the microstructure texture to get grains with high slip resistance [16]. Bahshwan et al. worked also with this steel and showed how the anisotropic microstructure leads to an anisotropic wear behavior [17][18]. Concerning the IN718, a large number of studies investigate the tribological behavior of this material when conventionally manufactured [19]–[22]. Most of the studies focused on the wear properties of the IN718 shaped by AM process are dedicated to the LPBF [23]–[25]. For instance, Samuel et al. [24] worked on the wear properties of IN718 manufactured by LPBF at high temperatures. They highlighted that the higher the temperature, the lower the wear resistance. Only very few articles treated the topics of the wear properties of IN718 deposited by LMD. Onuike et al. showed that the laser scanning strategy seems to have an impact on the wear properties but no further explanations were given [26]. Xu et al. showed that, by influencing the density, hardness, and microstructure, the laser power greatly changes the wear resistance of the IN718 [11]. Song et al. successfully enhanced the wear properties of this alloy by adding graphene particles to the material

during the LMD process. During the wear test, the graphene goes into the contact and acts as a lubricant, reducing the coefficient of friction (COF) and drastically lowering the wear rate [27]. Most of the articles concerning the wear of AM parts focused on the LPBF process. Moreover, IN718 is rarely taken as study material in these articles. So, the wear property of IN718 coating made by LMD is poorly documented and this is the objective of the present study.

In this work, our goal is to investigate the wear resistance of the IN718 deposited by LMD. With a view to quickly putting back the metallic part into service after coating and to limits costs, it was decided to apply a limited number of post-treatments. Only milling was applied (to control the surface topography), without further heat treatment. As, in a previous study [26], the scanning strategy turned out to be a critical parameter for wear resistance, we performed reciprocating sliding wear tests on samples manufactured according to four different scanning strategies. A tribological flat-on-flat contact was used for this study to produce a large contact area, which is representative of many industrial applications. Tests with different values of normal load and number of cycles were carried out to evaluate the impacts of these parameters on wear mechanisms. Finally, a comparative study was handled with a wrought IN718 to situate the competitiveness in terms of wear resistance of this same alloy manufactured by LMD. To better understand the wear behavior, we analyzed the evolution of the COF, the wear volume, the worn-surfaces of the two bodies and the modifications of microstructure (as-built and after tests).

2. Materials & Methods

2.1. Cladding of IN718 on a steel plate

The whole samples were built using a *BeAM* machine equipped with a 500 W YLR-fiber laser [28]. The powder used to manufacture the samples was provided by Oerlikon [29]. The powder was produced by gas atomization to give a final product composed of particles in a size range between 45 and 115 µm. The chemical composition of the IN718 powder and some of its properties are given in Table 1 and Table 2 respectively.

Table 1: Chemical composition of the material of the study

Elements	Ni	Cr	Fe	Nb	Mo	Ti	Al	Mn	Co	C	N	Si	S	O	P	Ca	Cu	Ta	Mg
LMD powder (Wt %)	Bal.	18.92	18.25	5.15	3.11	0.92	0.42	0.1	0.05	0.05	0.03	0.03	<0.01	<0.01	<0.01	<0.01	0.01	0.01	<0.01
Wrought (Wt %)	Bal.	18	18.5	5.2	3	0.9	0.5	N/A	N/A	0.04	N/A	N/A	-	-	-	-	-	-	-
100Cr6 pin (Wt %)	-	1.5	Bal.	-	-	-	-	0.4	-	1	-	0.25	-	-	-	-	-	-	-
XC48 substrate (Wt %)	-	-	Bal.	-	-	-	-	0.5-0.8	-	0.5-0.52	-	<0.4	-	-	-	-	-	-	-

Table 2 : Granulometric properties of the IN718 powder

Particles size distribution		
d_{10}	d_{50}	d_{90}
50 µm	67 µm	107 µm

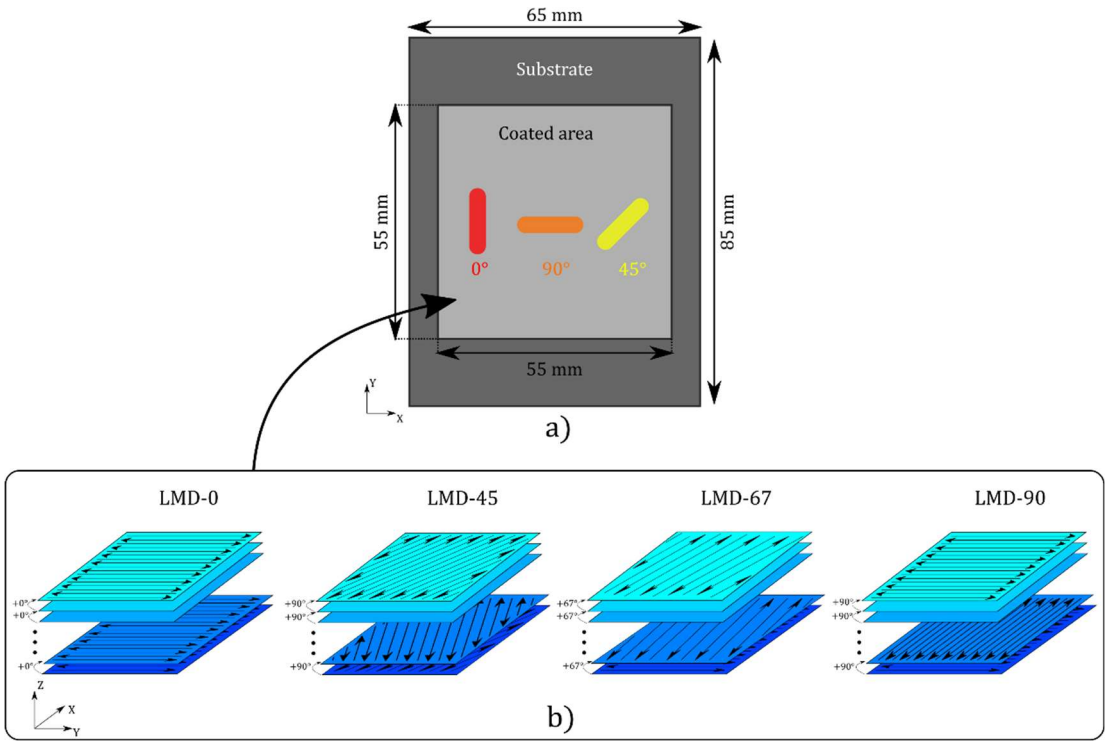

Figure 1 : a) Geometry of the samples; b) Schematic of the four scanning strategies

The coatings were performed on XC48 low alloyed steel plates with an initial dimension of 150 x 200 x 8 mm with the following process parameters: laser power of 325 W, a scanning speed of 2250 mm/min, a powder feed rate of 7 g/min, and an overlapping percentage of 30%. With such parameters, beads of about 200 µm high and 600 µm wide are deposited. In total, 4 square coatings of 2 mm high with different scanning strategies were deposited on one plate which represents the piling of 10 layers. Then, samples were split up using a band saw. As depicted in Figure 1 a), the final geometry of the samples consists of 55 x 55 x 2 mm coatings on top of plates with a dimension of 85 x 65 mm.

The four scanning strategies are displayed in Figure 1 b). The four strategies employ a back-and-forth motion of the laser but with different scanning directions and rotation at each new layer. Strategy 0° consists of a scanning direction parallel to one of the edges of the samples without any rotation of this direction. Strategy 45° and 90° have the same incremental rotation of 90° at each new layer but the initial scanning direction differs between both. Strategy 45° starts with a scanning direction that goes diagonally to the edge, whereas in Strategy 90°, the motion of the laser follows the edges. Finally, Strategy 67° has an initial scanning direction along the samples' edges and is subjected to an incremental rotation of 67° at each new layer. For each new batch of samples, all the coatings were built at the same location on the plate depending on their scanning strategy. As shown in Figure 2 a), initially, the as-built samples have a high roughness because of the unmelted particles sintered at its surface and the wavy topography induced by the overlapped beads. Therefore, to get rid of the high roughness surface and to ensure a good flatness, the surface of the samples was finally milled. It is worth noting that the milling process is the only post-treatment applied to the LMD coating. As the goal of this article is to study coating that allows one to quickly put back into service a worn metallic part, no heat treatments were performed. Therefore, the effect of different heat-treatments that could be applied after coating to change the microstructure and mechanical properties of the coating is not studied in this article.

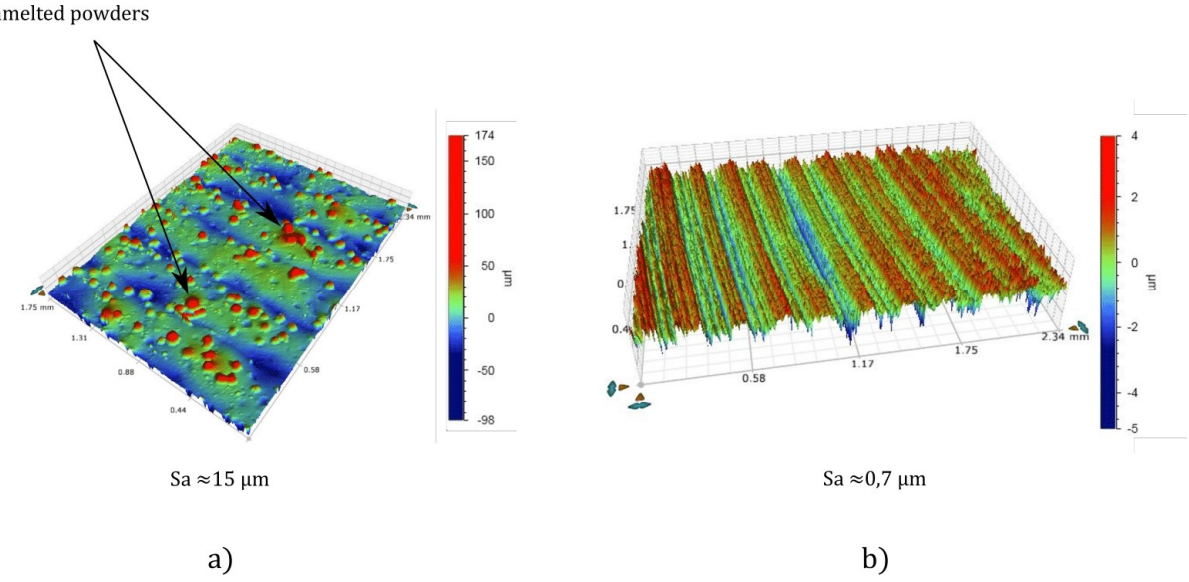

Figure 2: Samples roughness a) before and b) after milling

The milling parameters are given in Table 3. The use of this finishing process decreases the arithmetic roughness from 15 to 0.7 µm. As illustrated in Figure 1 b), because of the removal of 0.5 mm of material by milling, the final samples consist of 55 x 55 x 1.5 mm coatings.

Table 3: Milling parameters

Rotation speed (rpm)	Cutting speed (m/min)	Depth of cut (mm)	Depth of finishing cut (mm)	Table feed (mm/min)	Material of flutes	Number of flutes	Cutter diameter (mm)
95	23.87	0.2	0.1	29	Carbide	7	80

For comparison purposes, wrought IN718 cylinders (5 mm high and 20 mm radius) were used to perform wear tests radially. The composition of the wrought material is detailed in Table 1. The latter comes from a billet of IN718 (PYRAD53NW) supplied by Aubert&Duval [30]. For comparison purposes, the top surfaces of the wrought cylinders were milled as well with the same milling parameters given in Table 3.

2.2. Materials characterization before wear tests

A preliminary characterization of the tested materials was carried out before performing wear tests to better understand how their properties could impact their wear resistance. The microstructure, the density, and the hardness were analyzed through several characterization techniques detailed hereafter.

Before microstructural analysis of the surface contact, the specimens were polished by using SiC abrasive paper from 400 to 4000. Then a finishing polish was performed with a diamond paste of 3 and 1 µm. Finally, the specimens were electrolytically etched for 20 seconds at 5 V with a 20% diluted orthophosphoric acid. Metallographic observations of the top surface were performed with an *FEI QUANTA 600F* Scanning Electron Microscope (SEM). Electron Backscatter Diffraction (EBSD) maps were acquired as well, with an EBSD camera from *Oxford* [31]. The step size was set to 0.6 µm and the beam voltage was set to 30 kV for all the EBSD maps. The EBSD maps were post-treated with Aztec and Channel5 software [31]. The smallest grain has an area of 1.8 µm².

Hardness was measured with a *Zwick* machine [32]. Profile hardness underneath the milled surface was performed in diagonal in order to attain a step size of 10 µm. The first point of each profiles is located at 40 µm below the surface. A measurement consisted in applying a load of 750 mN for 5 seconds which results in an indent of 20 µm in diagonal. The mean values were calculated by averaging 3 profiles performed on the wrought and 4 profiles performed on the LMD samples (one on each strategy). The hardness is calculated through the software of the machine by using the Oliver-Pharr method [33]. The top surface hardness was measured using a Micromet5100 from *Buehler* [34] on the as-milled samples. For those measurements, 8 indentations were performed on each sample. They consisted in applying a load of 5 N for 15 seconds which gave an indent size neighboring 45 µm in diagonal.

To have an estimation of the density of the samples, image analysis was performed. A total of 6 transversal cross-sections of each sample were analyzed at different locations, after being polished with the same protocol as the metallographic observations. A total surface of 120 mm^2 was treated with the *ImageJ* software. The smallest porosity detected has an area of 2.5 μm^2. The mean density of the LMD samples was evaluated at around 99.9% for the four strategies.

Figure 3 summarizes the analyses performed on one of the LMD samples (LMD-0) and the wrought sample. The surface microstructure has already been studied in detail [35]. However, the most interesting features of this microstructure is described in the following paragraph. As shown in Figure 3 a), LMD sample top surface microstructure is heterogeneous with the alternation of small equiaxed grains and large columnar grains. The mean grain size calculated from this EBSD map is 24 ± 14 µm. A weak texture is also noticed which means that the grains are not oriented according to a specific direction. It is worth noting that the same heterogeneous top microstructure and mean grain size were observed in the three other LMD samples. Because of the significant cooling rate peculiar to the LMD process, a typical cellular/dendritic sub-microstructure is noticed in Figure 3 [36]. This rapid cooling rate is responsible for the presence of Laves phases observed in the interdendritic region as well. The heavier alloying elements (i.e. mainly Nb, Mo, and Ti) are segregated in the interdendritic region during the solidification which is the main reason why Laves phases are found in the wall cells [37]. No strengthening phases (γ' and γ") were observed by SEM. Although SEM is not the best characterization method to capture those small precipitates, none of them were expected to be found in the LMD samples because of the combination of the sluggish precipitation kinetics of those phases and the high cooling rate [36], [38]. As shown in Figure 3 c), the wrought sample has a more homogeneous microstructure than the LMD sample with an even lower texture than the LMD samples. With a mean grain size of 6 ± 5 µm, the wrought IN718 has a finer microstructure than IN718 processed by LMD as well. In Figure 3 d), the classical δ acicular precipitates in wrought IN718 were observed by SEM in the grain boundaries. Some carbides were observed as well. However, no strengthening phases were noticed by SEM. The wrought hardness is on average lower than LMD despite its finer microstructure and the most likely precipitation of strengthening phases. In the bulk of the samples, the mean hardness of the wrought sample is 265 ± 12 HV, whereas for the LMD samples, their hardness is 336 ± 11 HV. This difference, in favor of the LMD samples, can be explained by the considerable amount of dislocations inside the as-built LMD samples compared to the fully recrystallized conventionally manufactured samples [39], [40]. Such difference of hardness was already reported by Nguejio et al. with the IN625 [41].

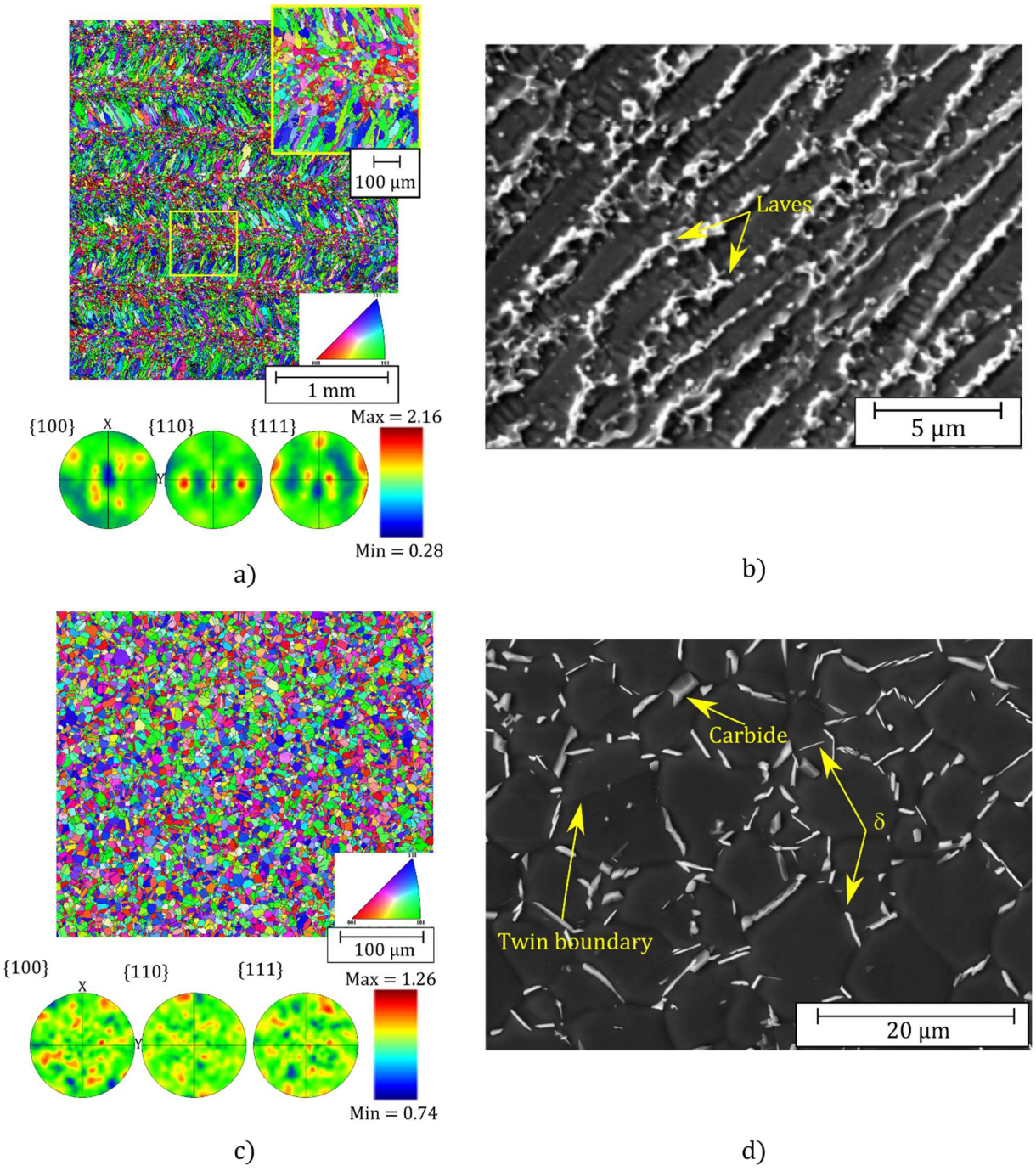

Figure 3 : EBSD (IPF Z) map and SEM picture of the top surface of a,b) LMD (Strategy 0°) and c,d) wrought sample.

2.3. Wear tests

Reciprocating sliding wear tests were undertaken with a homemade bench depicted in Figure 4. It is composed of a stationary arm upon which weights are stacked to get the desired normal load. This arm carries the tangential force sensor and the pin holder. The counter-body material and its geometry have been chosen to ensure the wear of the coating while having flat-on-flat contact. Therefore, the flat face of the 100Cr6 pin has been taken as a counter-body. Its hardness is about 840 HV and its chemical composition is given in Table 1. The pin is 15 mm long and, as illustrated in Figure 4, it has a radius of 3 mm with a fillet of 0.5 mm. The pin is located at the extremity of the arm, straight underneath the stacked weights. Underneath it, an oscillating plate receives the

sample which is fastened with two screws. The plate is equipped with an adaptive piece (the green piece in Figure 4) which allows the positioning of the samples in three different directions: 0, 45, and 90° as shown in Figure 1 a). Before testing, the pin is subjected to an *in situ* grinding in order to ensure the good match of the two surfaces in contact. This step consists of interposing a P400 SiC grinding paper between the pin and the sample while the plate is oscillating at 1 Hz for 2 minutes. The final topography of the pin is shown in Figure 4. The roughness of the pin before testing is about Sa = 0.4 µm. All tests were performed three times for each different tribological conditions.

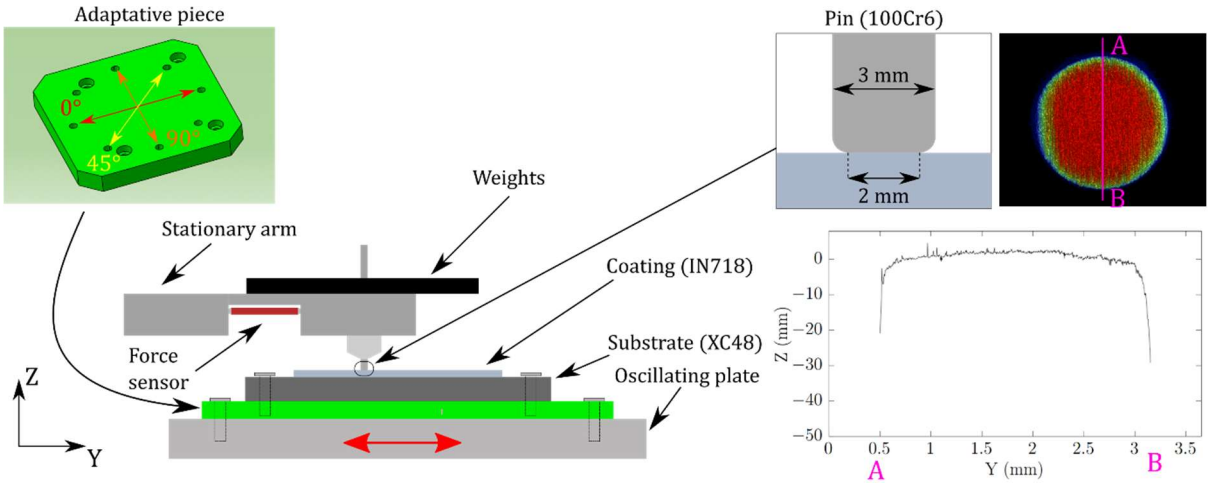

Figure 4 : Schematic of the reciprocating sling bench test with a zoom on the pin geometry

The tangential force is acquired as a function of the position for each cycle with an acquisition frequency of 600 Hz. The COF is calculated for each cycle by averaging the tangential force (F_t) obtained without counting the turnaround points. Also, the total dissipated energy (E_d) of a wear test of N cycles is calculated by using the following classic Equation (1):

$$E_d = \sum_{i=1}^{N} E_{d,i} = \sum_{i=1}^{N} \int_{-\delta^*}^{+\delta^*} F_t(\delta) d\delta \quad (1)$$

With δ* the stroke length and δ the position.

The whole used tribological parameters are summarized in Table 4. The tests were carried out at room temperature (around 20°C) and with a relative humidity of about 30%. It can be noted from Table 4, that the stroke length and the frequency are 10 mm and 3 Hz respectively. They are the only parameters that never change in all the tests.

Table 4: Constant and variable tribological parameters used for each study

Studies	Constant parameters		Variable parameters	
Impact of scanning strategy, sliding direction and normal load on wear	Frequency (Hz)	3	Normal load (N)	2, 20
	Stroke length (mm)	10	Sliding direction	0°, 45°, 90°
	Number of cycles	5 000	Scanning strategies	0°, 45°, 67°, 90°
Impact of the number of cycles on wear	Normal load (N)	20	Scanning strategies	0°, 67°
	Frequency (Hz)	3		
	Stroke length (mm)	10	Number of cycles	5 000, 20 000, 40 000, 50 000, 100 000
	Sliding direction	0°		
Comparison between the wear resistance of wrought and LMD samples	Frequency (Hz)	3	Normal load	2, 20
	Stroke length (mm)	10	Scanning strategies	0°, 45°, 67°, 90°
	Number of cycles	5 000	Sliding direction	0°, 45°, 90°

2.4. Wear quantification and analysis

To evaluate qualitatively and quantitatively the wear of our samples and the counter body several characterization techniques were employed. The wear volume on the LMD samples was measured by using an interferometer GT-K1 from Bruker [42]. The whole wear track was scanned with a green light in order to have the most accurate wear volume as possible. Figure 5 defines the wear volume. It corresponds to the volume of material removed from the coating's surface by taking as surface reference the milled surface. Therefore, the adhered wear debris are not considered in the measurement of the wear volume. The debris present at the interface during the test and removed by the samples cleaning before interferometric measurement are considered in the wear volume (Figure 5 b). We have actually no way to quantify the amount of wear debris that were present at the interface, before being ejected from the contact, and they could have acted either as a solid lubricant (and allow for smaller rates of material lost) or as an abrasive (and increase the rate of material lost).

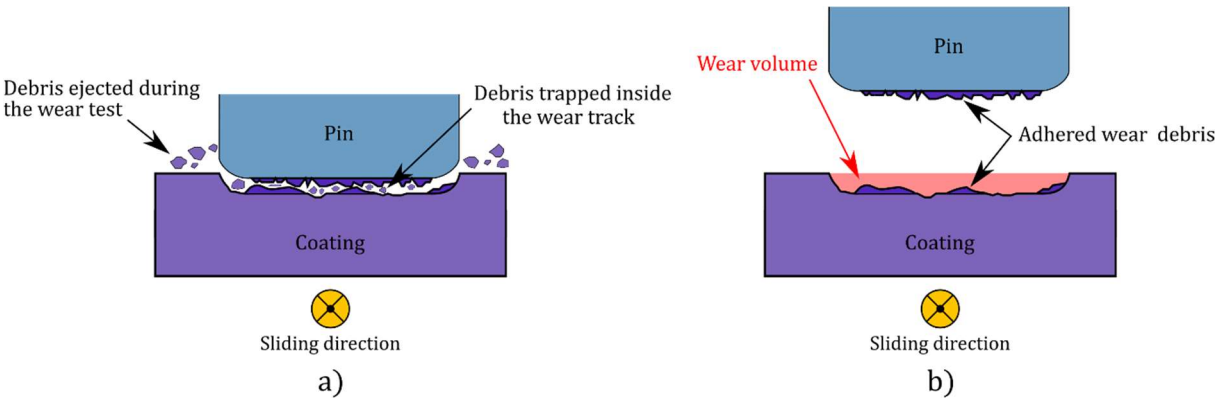

Figure 5: a) Cross-section of the wear scar during the wear test ; b) Drawing defining the wear volume after the wear test (after cleaning)

The wear tracks, the pin surface and the wear debris were observed by SEM and with an VHX6000 optical microscope from *Keyence*. Finally, SEM observation were completed with Energy Dispersive X-ray spectroscopy (EDX) with the use of a detector from *Oxford* [31]. Cross-section analysis of the wear track were performed as well by SEM. Kernel Average Misorientation (KAM) maps were performed underneath the wear track to evaluate

the depth of strained area induced by the wear tests as well as observe the stacking of the defects. In order to avoid the work-hardening caused by the mechanical polishing, a cross-section ion-polishing in PECS II *Gatan* has been performed at 8 keV for 8 h. The EBSD acquisition parameters are the same as the ones used to perform the metallographic observation of the contact surface. The calculation of KAM maps was done by taking in count the first neighbors.

We calculated the wear rate (k, in mm^3/Nm) of the wear tests by using the Equation (2) (Archard's law) as follow:

$$V = k * F_N * L \quad (2)$$

With V the wear volume (mm^3), F_N the normal load (N), and L the total length traveled by the pin (mm).

3. Results & Discussion

The results are organized in three parts. In all those parts, the goal is to identify how the process and tribological parameters impact the wear behavior of the tested samples and to point out the key phenomena. First, the impacts of the scanning strategy and the sliding direction are studied for several values of normal load. Then, the evolution of wear with the number of cycles is investigated. Finally, the wear resistance of the LMD samples is compared to the one of a conventionally manufactured IN718.

3.1. Impacts of the scanning strategy and sliding distance on wear

The evolution of the coefficient of friction (COF) is displayed in Figure 6 a). At 20 N, no matter which strategy was employed to deposit, the COF remains steady at around 0.65. The COF at 2 N is slightly higher with a mean value of 0.69. This highest value of the mean COF is primarily due to the appearance, after a certain number of cycles, of a steady state of the evolution of the COF. Figure 6 b) highlights the more significant standard deviations and the highest mean value of the COF for the tests performed at 2 N which proves the unsteadiness of the COF with such a normal load. The volume loss induced by the reciprocating wear tests of the LMD coatings in several conditions is shown in Figure 6 c). When a normal load of 20 N is applied, no significant differences in wear volume are observed between the four different strategies. It emphasized also that the sliding direction does not impact the wear behavior of the deposited part. At 2 N, despite some discrepancies in the mean wear volume, those differences go along with large error bars. Also, by the means of both Y axis, no proportional relationship was found between the wear volumes obtained at 2 and 20 N. So, it can be stated that the scanning strategy and the sliding direction do not affect the wear even at a low normal load. The same conclusion can be drawn by examining the wear rates associated with different tribological conditions in Table 5. For example, when subjected to a load of 20 N, the wear rates consistently remain at approximately $6.5*10^{-4}$ mm^3/Nm, irrespective of the chosen scanning strategy or sliding orientation. By reasoning in terms of "wear coefficient", i.e. multiplying the wear rates by the hardness of the softer body, we obtain a wear coefficient of around $2.9*10^{-3}$. Archard et al. supports the notion that such a wear coefficient is typical of a metal/metal dry contact which is close to our pairing [43]. Other articles have investigated the wear rate of alloys when they are shaped using additive manufacturing processes. Riza et al. studied 316L steel and H13 tool steel, and observed wear rates of approximately 10^{-5} mm^3/Nm [44]. Anandakrishnan et al. studied the wear of IN718 shaped by Direct Metal Laser Sintering and subsequently heat-treated [45]. They found wear rates that were also close to 10^{-5} mm^3/Nm. The fact that the wear rates we obtained are one order of magnitude higher can be explained by the contact geometry. Using a polished pin with a diameter of 3 mm strongly promotes adhesive phenomena, leading to a more significant wear volume [46]. Although the fact that the scanning strategy does not affect the wear behavior, which is contradictory to Onuike et al. [47], logical explanations of this result were found in this investigation.

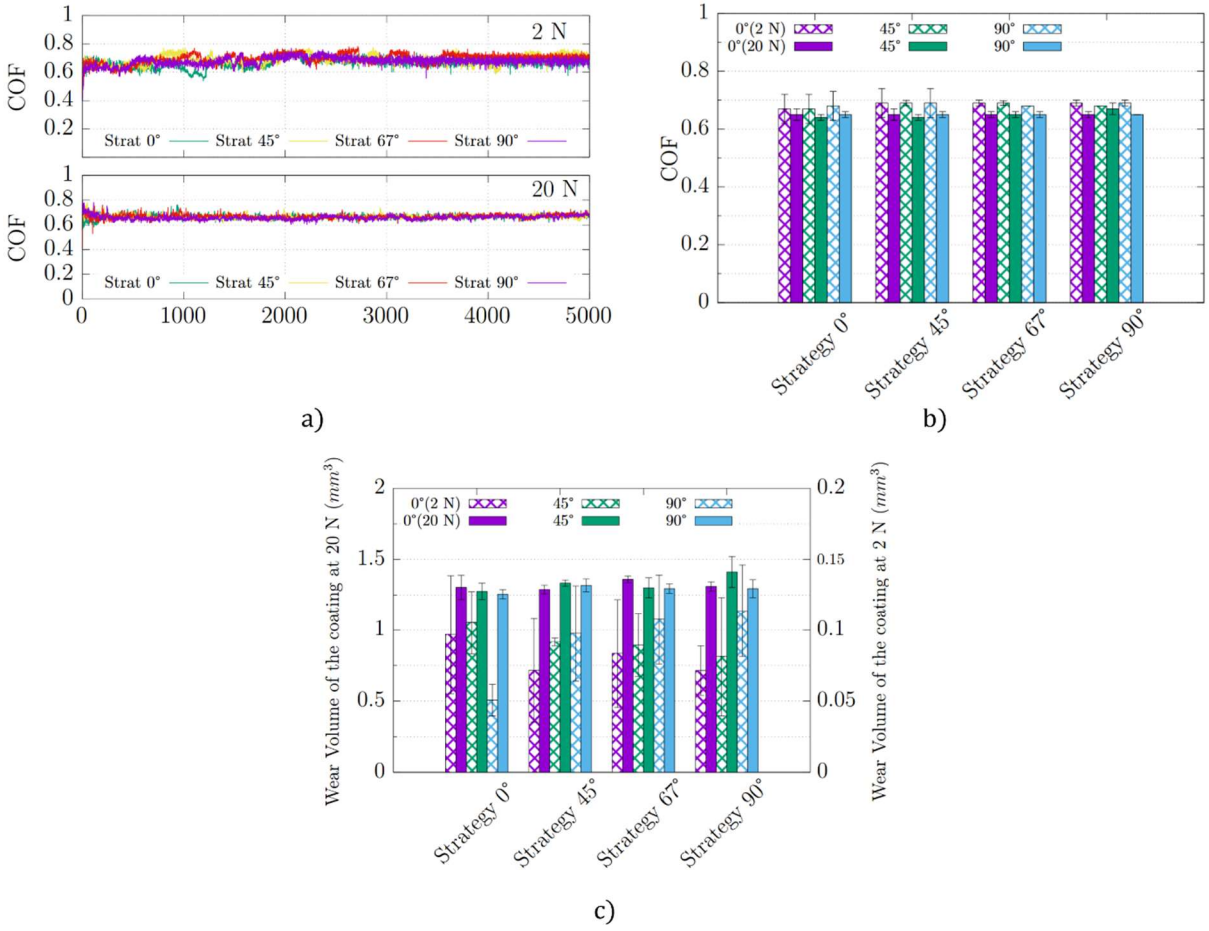

Figure 6: a), b) and c) give information on the evolution of the COF, the mean COF and the wear volume of the coating respectively for different loads, sliding directions and scanning strategies. The crosshatched and filled bars indicate results for the tests performed with 2 N and 20 N normal load respectively. Each color represents a specific sliding direction.

Figure 3 a) showed a highly heterogeneous microstructure at the mesoscale which leads to local hardness variation which would lead us to believe that the strategy could impact wear [35]. However, in our case, as the contact chosen is a large surface contact (around 3.14 mm²), it embraces a large number of grains. Therefore, during the wear tests, the pin does is not sensitive to the local heterogeneities at a lower scale. Instead, the mechanical properties of the deposited part are averaged by the large area covered by the pin. It means that the inherent anisotropy of the mechanical properties of the AM part might be ignored as long as the contact area is larger than the local microstructural heterogeneities. Several articles dedicated on the 316L manufactured by Laser Powder Bed Fusion (LPBF) highlighted the anisotropic wear properties of their parts [15], [17], [18]. However, in those cases, the contact size was much smaller and so, the wear tests were more prone to be affected by microstructural features at a smaller scale. In our case, the microstructure of the IN718 deposited by LMD does not vary (except for the orientation of the periodic pattern of small and large grains). This explains why neither the scanning strategy nor the sliding direction impacts the wear behavior of our coatings.

Table 5 : Result of wear rates for different scanning strategy and sliding direction

Wear rates (*10^{-4} mm^3/Nm)						
Normal load	2 N			20 N		
Sliding direction	0°	45°	90°	0°	45°	90°
Strategy 0°	4.85 ± 2.09	5.26 ± 1.11	2.54 ± 0.56	6.52 ± 0.43	6.38 ± 0.29	6.28 ± 0.16
Strategy 45°	3.58 ± 1.82	4.58 ± 0.14	4.89 ± 1.69	6.45 ± 0.15	6.67 ± 0.11	6.59 ± 0.23
Strategy 67°	4.18 ± 1.91	4.47 ± 1.10	5.38 ± 1.58	6.80 ± 0.11	6.51 ± 0.35	6.48 ± 0.17
Strategy 90°	3.57 ± 0.87	4.07 ± 2.09	5.69 ± 1.63	6.55 ± 0.16	7.06 ± 0.55	6.48 ± 0.32

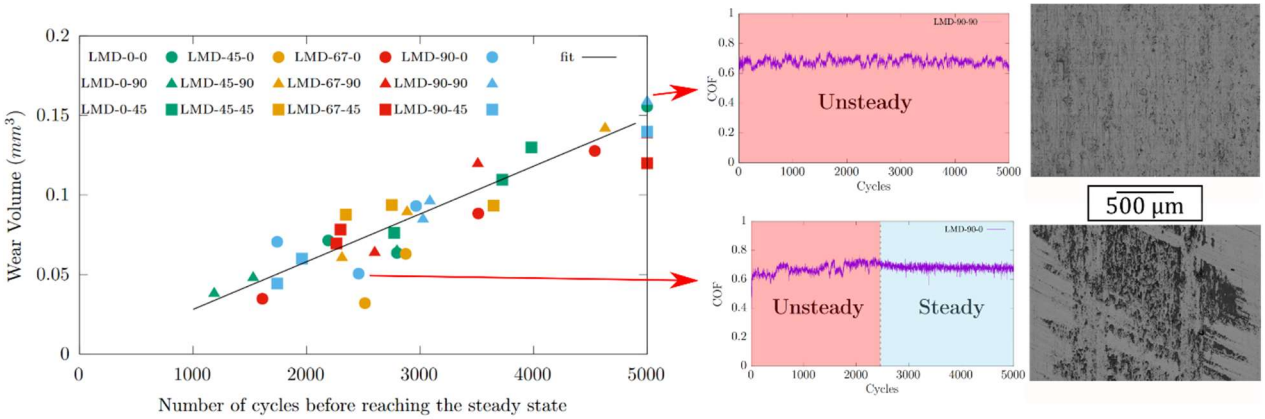

Figure 7: Correlation between the wear volume, the evolution of the COF, and the wear mechanisms for wear tests performed at 2 N. The naming system in the key area can be read as follow: LMD-Strategy-Sliding direction.

It can be noticed in Figure 6 a) that, for the tests performed at 2 N, a steady state appears. However, this stabilization of the COF seems to not appear after a fixed number of cycles. To sort the tests according to when the COF stabilizes, the starting cycle of the steady state was calculated for each test. To dissociate an unsteady state from a steady state in the COF evolution, a systematic method was employed. First, the average COF of the 100 last cycles is calculated. Then, starting from the last cycle, this value is compared with the COF of every cycle. Since the difference does not exceed 5% (this percentage has been chosen empirically as it gives the most accurate results after analyzing carefully different tests), the trend of the COF is still considered as steady. Otherwise, it means the COF switches to an unsteady state.

Figure 7 shows the evolution of the wear volume as a function of the starting cycle of the steady state. From this graph, it can be stated that the latter the steady state appears, the larger the wear volume. Moreover, this evolution of wear has a linear trend. Given how scattered the results obtained by the tests performed on the sample with the same strategy or the same sliding direction are, it can be concluded that this phenomenon is not dependent on those parameters. To better understand why the tests possessing a steady state have a lower wear volume, two cases were isolated as depicted in Figure 7. The first case is a test leading to a high wear volume whereas the second case is illustrated by a test having more than half as much wear volume as the first case. The first case never reached the steady state and the main wear mechanisms observed are abrasion and adhesion. For the second case, a steady state appears around the 2500th cycle. After 5000 cycles, the main wear mechanisms noticed are abrasion and oxidation of wear debris. The oxides are highlighted in Figure 8. The oxides are cracked with cracks perpendicular to the sliding direction. Those cracks can be explained by the brittleness

of the oxides which do not withstand the traction stresses imposed by the sliding contact. From those results, a clear correlation between the steady state of the COF and the presence of highly oxidized debris can be drawn. As given in Table 6, the EDS measurement performed inside the oxide (1) highlights a large amount of oxygen combined with iron, chromium, and nickel, whereas outside the oxide (2), the classical composition of the IN718 appears.

Figure 7 allows to state that the latter the steady state appears (i.e. the oxidized transfer layer), the more the LMD sample is worn. From those results, it can be concluded that when oxides remain in the contact, the latter act as a protective layer which prevent the wear of the coating.

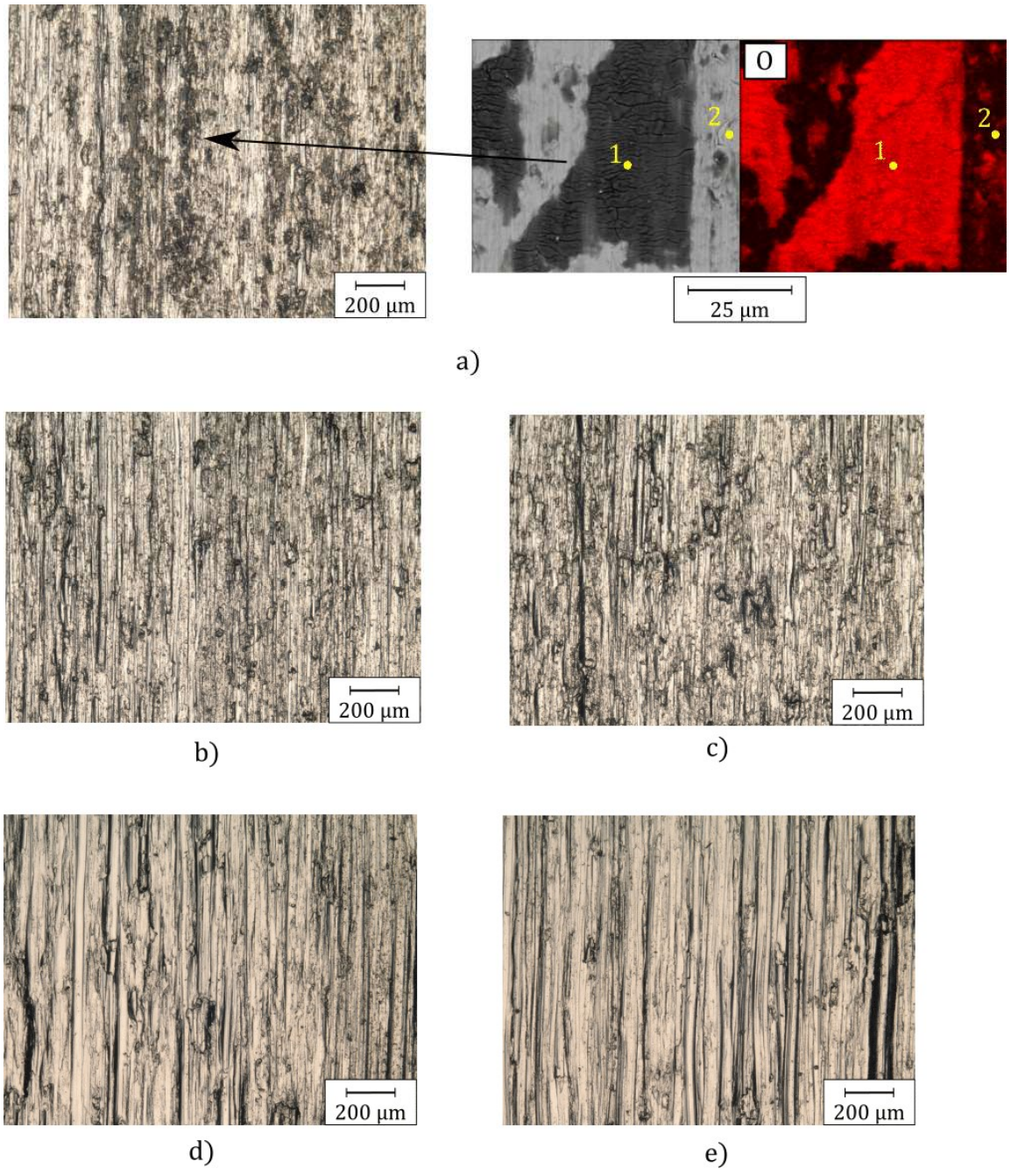

Figure 8: Optical images of worn surfaces of the LMD samples at a) 2 N (with a steady state of the COF); b) 10 N; c) 20 N; d) 40 N; e) 50 N

Several wear tests with different loading conditions were performed. Figure 8 gathers the optical pictures taken inside the wear track. As seen previously, at 2 N, abrasion is the main wear mechanisms (Figure 8 a)) and oxidized wear debris are present as transfer layer. At 10 N, the oxidized transfer layer disappears to make way for abrasion and adhesion. As exposed in Figure 8 b), narrow and shallow grooves are observed inside the worn area with adhered debris. At 20 N, the same observations are noted. Starting from 40 N, it can be noticed in Figure 8 d) and e) that the wear is mainly due to abrasion with much less adhesion. Thick and deep grooves inside the wear tracks are observed with some big debris which are cold-welded.

Table 6 : EDS measurements performed inside the wear track shown in Figure 8 a)

Element		O	Ni	Fe	Cr	C	Nb	Mo	Ti	Mn	Al	Si
1	Wt%	29.22	31.2	15.08	12.51	5.44	3.24	2.16	0.61	0.26	0.24	0.06
	σ	0.07	0.08	0.05	0.04	0.09	0.04	0.05	0.02	0.03	0.01	0.01
2	Wt%	3.46	48.39	16.61	18.13	3.6	5.16	3.06	0.88	0.26	0.35	0.1
	σ	0.04	0.09	0.06	0.05	0.09	0.05	0.06	0.02	0.03	0.01	0.01

Table 7 : EDS measurements performed on the surface of the pin shown in Figure 9 b)

Element		O	Ni	Fe	Cr	C	Nb	Mo	Ti	Mn	Al	Si
3	Wt%	0.6	2.1	92.4	1.7	2.6	0	0.1	0	0.4	0	0.2
	σ	0.1	0.4	0.5	0.1	0.1	0.1	0	0.1	0.1	0	0
4	Wt%	5.4	50.2	16.8	16.5	2.5	4.6	2.8	0.7	0	0.4	0.1
	σ	0.1	0.4	0.2	0.2	0.2	0.1	2.8	0.7	0.1	0	0

Figure 9 shows the contact surface of the pin after the wear tests. As expected, when a 2 N load is applied, oxides are found on the pin's surface as well. It can be also noted that, under those conditions, not the entirety of the pin's surface was in contact with the coating. Indeed, an unworn area is observed at the rim of the pin. This phenomenon is not noticed anymore when the applied load exceeds 10 N. 10 N, adhered debris were found at the surface of the pin but without covering the whole surface. EDS analysis, given in Table 7, highlights the presence of nickel and some alloying elements of the IN718 at the surface of the pin which proves that adhesion happens. However, the point (3) demonstrates that not the whole surface of the pin is covered by debris at 10 N. Large bands parallel to the sliding direction left the 100Cr6 uncovered. Then, as the applied load increases, the fewer those uncovered areas are. As observed in Figure 9 d) and e), from 40 N, the pin's surface is completely covered by IN718 debris leading to a complete transferred IN718/IN718 contact. The mass difference of the pin was monitored as well. From those measurements, the main information to retain is that, starting from 20 N, the pin gains the same mass (a gain of 0.2 mg) which means that even at 50 N, the mass gain is the same. It can be assumed that after reaching a certain thickness, the transferred layer can no longer mechanically sustain the stresses imposed by the sliding contact. Thus, since this critical thickness is attained, the latter will remain constant no matter the load applied or the number of cycles of the test. In Figure 10, Scanning Electron Microscopy (SEM) pictures feature the differences in wear mechanisms but also in terms of debris size and geometry. Indeed, the debris obtained after a wear test with a normal load of 20 N are small plate-like debris whereas the debris collected after a wear test with a load of 50 N are large with an elongated shape. The plate-like geometry has been already reported by Thirugnanasambantham et al. [48] which is the result of the deformation and the compression of the surface. The size of the debris is probably larger as the load increases because it results in deeper plowing and on a long distance of sliding.

Interestingly, as shown in Figure 11, the wear follows an increasing linear trend as a function of the dissipated energy linked to the normal load. Also, the small error bars are the witnesses of the high repeatability of the

wear tests (a minimum of 3 tests were performed for each tribological conditions). It can be noticed that, at this scale, the variation of the wear volume observed at 2 N in Figure 7 seems to be derisory.

Thanks to those results, the observed tribological phenomena can be schematically synthesized. The evolution of the wear mechanisms according to the applied normal load was summarized in Figure 12. At low load (i.e. 2 N), the wear is mainly driven by abrasion and oxidized transfer layer is present. Because of the low normal load inducing low shear stress, the latter is not large enough to pull out the oxide patches. Thus, a highly oxidized debris remains inside the contact and creates a protective transfer layer which will wear instead of the coating. As observed in Figure 7, those patches act as a protective layer. Thus, the sooner this protective layer appears, the lower the wear volume. Then, from 10 to 20 N, the main wear mechanisms are abrasion and adhesion. The coating is worn by the small IN718 work-hardened abrasive debris which are trapped inside the contact. Those debris come from the delamination of IN718 fragments. Some of the debris are cold-welded either in the wear track or on the pin's surface. At this load, the latter is almost entirely covered by IN718 debris. Finally, from 40 to 50 N, although adhesion remains one of the main wear mechanisms, it seems to fade into the background compared to the abrasion. From those tests, bigger wear debris from the coating are created. These large and hard debris are responsible for the plowing of the samples' surface resulting in large and deep grooves with some large debris welded sporadically at the surface of the worn-out area.

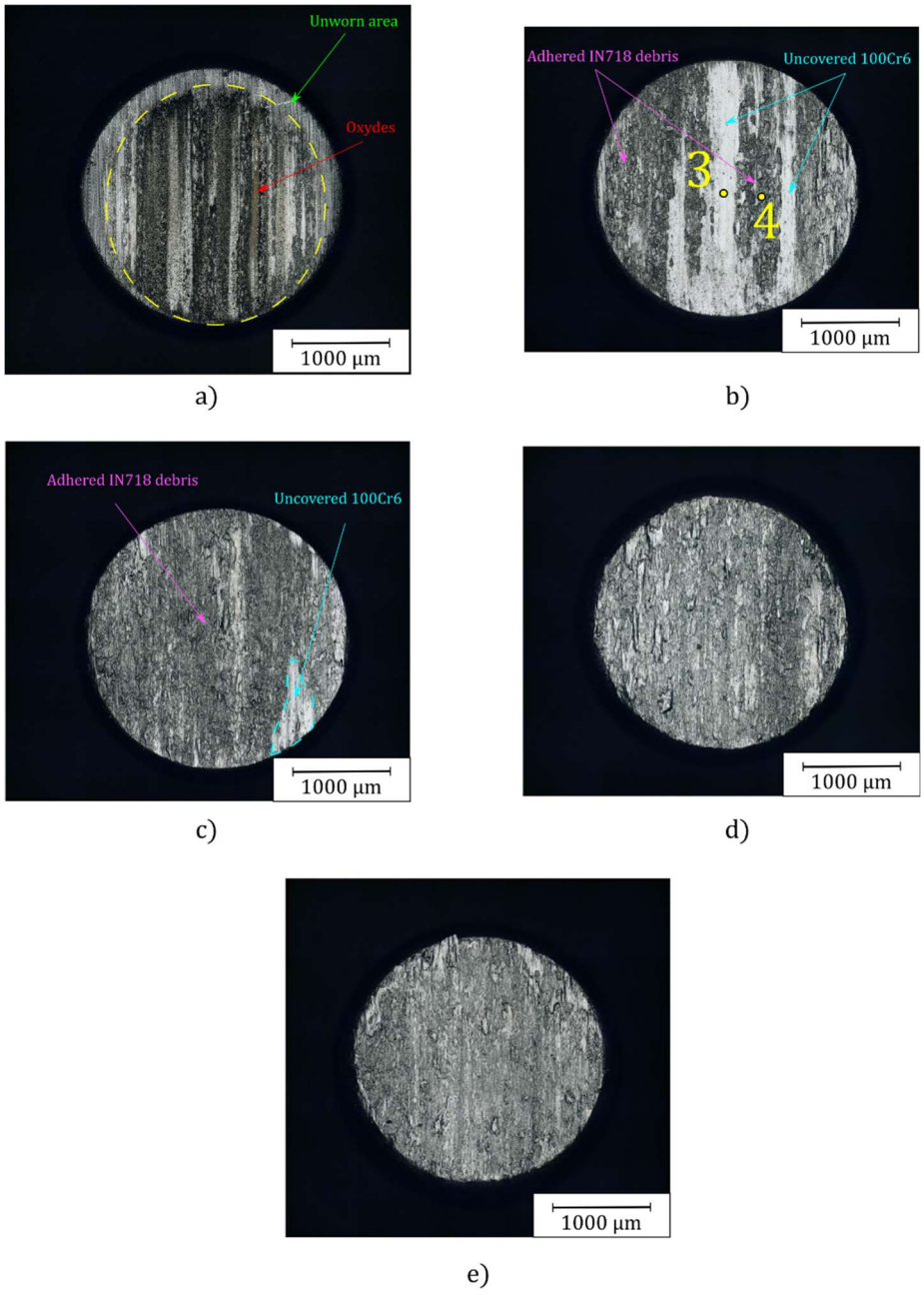

Figure 9: Optical images of the contact surface of the 100Cr6 pin after wear tests performed at a) 2 N; b) 10 N; c) 20 N; d) 40 N; e) 50 N

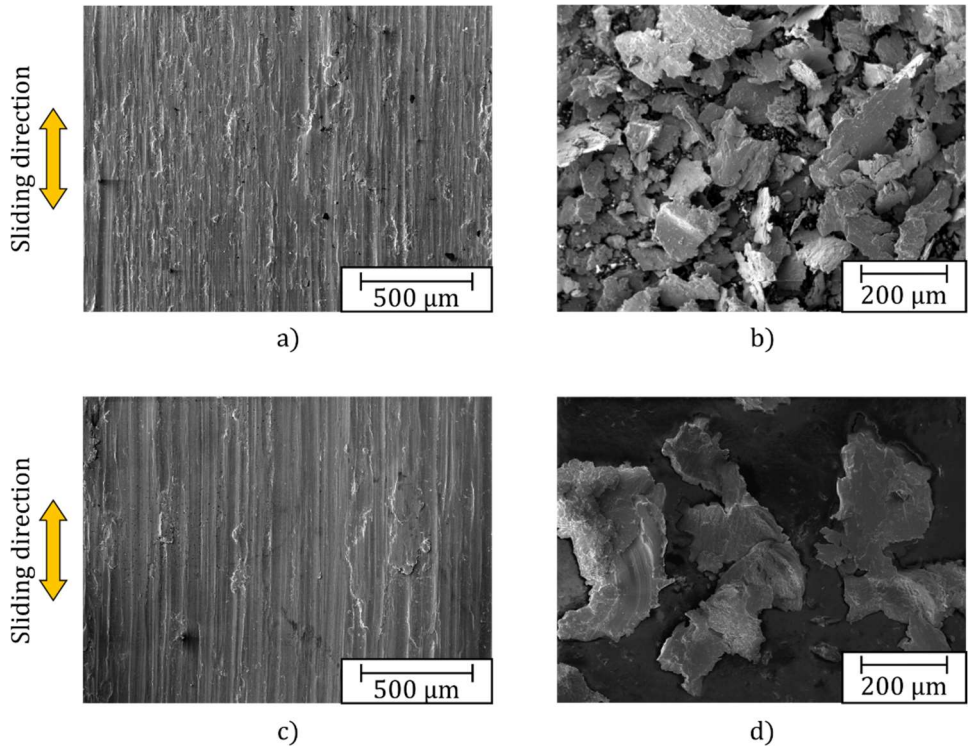

Figure 10: SEM pictures (secondary electrons detector) of the worn area and the debris induced by the wear tests performed with an applied load of a) and b) 20 N; c) and d) 50 N

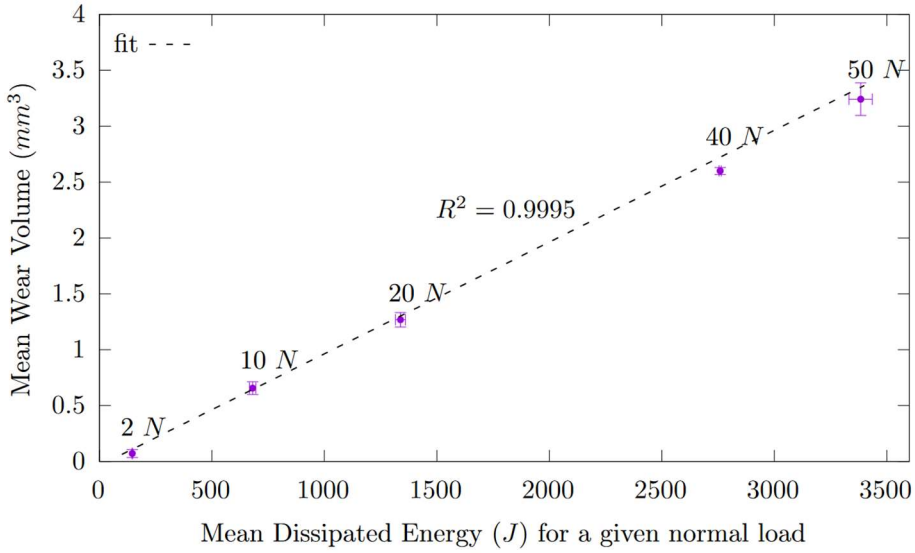

Figure 11: Mean wear volume as a function of the mean dissipated energy

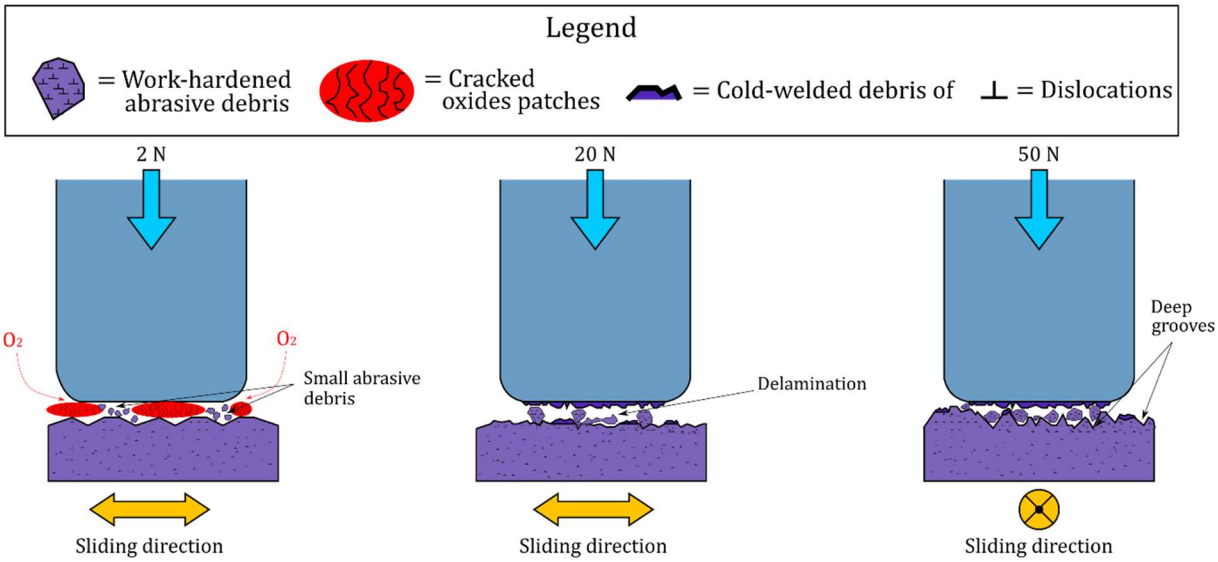

Figure 12: Evolution of the wear mechanisms depending on the normal load applied

3.2. Wear evolution with the number of cycles

Since wear was previously studied for a constant number of 5000 cycles, the evolution of wear over time is now examined. It has been observed lately, that, after performing a reciprocating sliding wear test of 5000 cycles, the top surface microstructure induced by the different scanning strategies does not impact the wear volume. However, these tests do not ensure to remove enough volume to encounter, at least, one layer/layer interface. It has been shown in the literature that during a tensile test, the maximal strain happens at the interface between layers [49]. Thus, as the interface between layers seems to have specific mechanical properties, longer tribological tests were performed to see if the interface plays a role in the wear behavior of the LMD samples. Moreover, those tests will ensure to wear below the region where the microstructure was strained by the milling process (estimated at 100 µm underneath the surface).

The evolutions of the COF of 2 wear tests for different numbers of cycles are shown in Figure 13. Until 20 000 cycles, a stable evolution of the COF is observed with a mean value of 0.69. Then, from 20 000 cycles, the evolution of the COF starts to become less steady with a slight drop of the COF around 0.6. Interestingly, as displayed in Figure 14 a), after several cycles (in the range between 40 000 and 50 000 cycles), the wear volume stops increasing and remains the same. As shown in Table 8, the wear rates decrease with time. The wear rate starts with an initial value of $7*10^{-4}mm^3/Nm$ for the first 20 000 cycles. Then, it starts to decrease until 50 000. After 50 000, the wear rate becomes non-significant (i.e. close to 0). This phenomenon is shown in Figure 14 a), where the wear volume reaches a plateau above 50 000. On the other hand, as displayed in Figure 14 b), the mass loss of the pin never stops to increase. Those first results testify that, after a certain amount of time, the counter-body stops wearing the coating and starts to wear itself on the coating surface. Also, even after long wear tests, no differences in terms of wear were observed between the two LMD samples with different scanning strategies. As shown in Figure 15 a), after 20 000 cycles, the pin had barely encountered the layer/layer interface. However, after 50 000 cycles (Figure 15 b)), the pin passed through several of them. As the wear volume keeps increasing until 50 000 cycles despite encountering the interface, it can be stated that the latter does not impact the wear behavior. Moreover, given that after 100 000 cycles, the pin surely encounters at least one time the interface between two layers (i.e. the wear depth is higher than the layer thickness) and because the wear volume is approximately the same for both strategies, it can be stated that in addition of the interface, the scanning strategy does not impact wear behavior as well.

To better understand the trend of the evolution of the wear volume as a function of the number of cycles, the surface of the worn-out area of the LMD samples and the pins were investigated and displayed in Figure 16 and Figure 17 respectively. After 20 000 cycles, the wear mechanisms are the same as those reported previously, i.e. abrasion and adhesion. It can be observed in Figure 16 a) that no oxides were detected at the surface. Inside the wear track, smeared oxidized IN718 wear debris, and grooves are seen. By looking at the surface of the counter-body in Figure 17 a), as for 5 000 cycles wear tests, oxidized adhered-debris of IN718 were found. However, the percentage of the surface occupied by the wear debris appears to be less substantial than the counter-bodies used for the wear tests of 5 000 cycles (Figure 6 c)). This assessment is in agreement with the evolution of the mass difference in Figure 14 b). Indeed, the mass difference of the pin after 20 000 is still positive; however, it is lower than after 5 000.

Starting from 50 000 cycles, wear mechanisms change. An oxidized transfer layer appears at the surface of both bodies in contact. From the top, the distribution of the oxides in the wear track is not homogeneous (Figure 16 b)). From a transverse point of view (Figure 16 c)), it can be noticed that the thick oxides do not cover entirely the surface of the wear track. Also, the plastic deformation induced by the contact is less discernible than after 20 000 cycles where deformed cells could be noticed. The presence of oxygen on the pin comes from two phenomena: classically from the adhesion of oxidized debris but also the oxidation of the pin. As shown in Figure 17 b), the left part is rich in iron and oxygen with a depletion of nickel whereas, on the right part, the EDS mapping highlights an area rich in oxygen and nickel which corresponds to oxidized IN718 debris. At this stage, according to Figure 14 a), the coating stops wearing and the counter-body is worn instead. Despite the presence of adhered debris on the pin, at this number of cycles, the pin has undergone a high loss of mass. It might mean that the adhered debris found at its surface is not meant to remain. Finally, after 100 000 cycles, highly oxidized wear tracks are seen. In Figure 16 c), the backscattered electron picture acquired with the SEM highlights the well-spread oxide layer inside the wear track. Also, the cross-section of the track shows that the oxide layer is thinner than after 50 000 cycles. Concerning the pin, the adhered debris become rarer and the pin's surface is mainly covered by iron oxides.

From those observations, it can be stated that the protective oxidized layer has a critical role in the wear properties of those coatings. First, as the COF tends to slightly decrease when oxidation occurs, it can be assumed that this layer acts as a solid lubricant. Also, we observed previously in Figure 8, that this oxidized layer is cracked, which shows its brittle behavior. Thus, it can be assumed that this protective oxidized layer on the plane has a high hardness which protects the coating but wears the pin (as shown in Figure 14 b and c). Eventually, the unsteady evolution of the COF after 20 00 cycles may be associated with repeated formations and eliminations of this protective layer. From those analyses, the whole picture of the evolution of wear with time is summarized in Figure 18. Before 20 000 cycles, only the coatings are worn-out by the pin. At this stage, the wear volume is almost proportional to the number of cycles. The main wear mechanisms are abrasion and adhesion. Then, as the number of cycles extends to 50 000 cycles, the wear rate decreases. Thick oxides appear irregularly inside the wear track. Those protect the surface of the samples and wear the pin instead. However, wear of the coatings still happens because of the incomplete coverage of the oxide at the surface of the worn-out area of the coatings. It is only above 50 000 cycles that wear of the LMD samples reaches a steady state because of the full coverage of the oxide protective layer. The appearance of oxide is still not fully understood. It might be explained by the increase of oxygen content inside the contact over time that might facilitate the oxide formation.

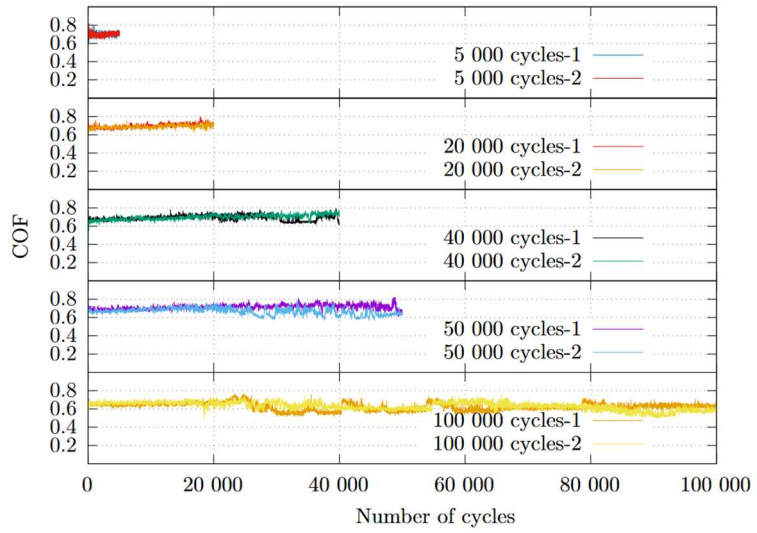

Figure 13: Evolution of the COF as a function of the number of cycles

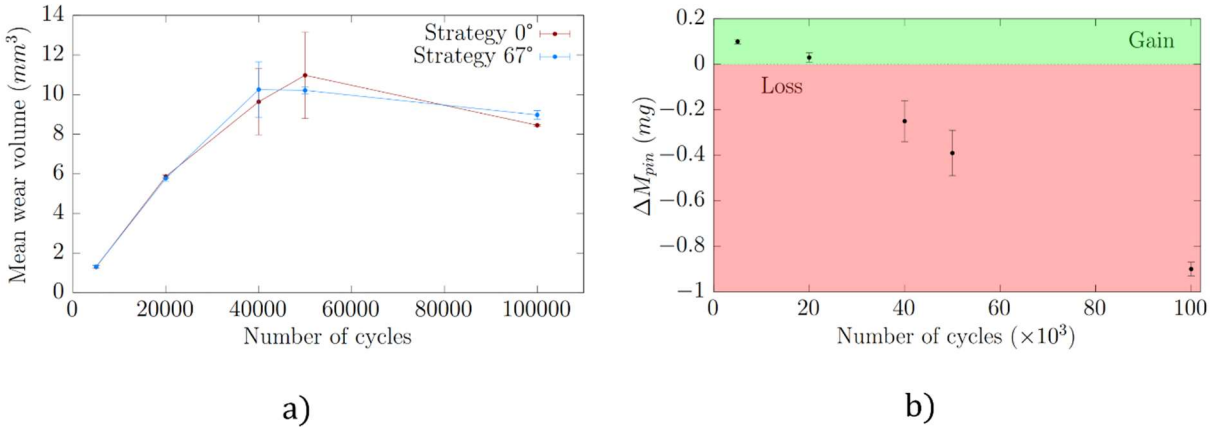

Figure 14: a) Mean wear volume of the coating; b) Mass difference of the pin as a function of the number of cycles (Test performed with: Fn = 20 N; f = 3 Hz; t = 5000 cycles)

Table 8 : Result of wear rates according to the number of cycles

Wear rates (*10^{-4} mm^3/Nm)					
Number of cycles	0 to 5000	5000 to 20 000	20 000 to 50 000	50 000 to 100000	0 to 100 000
Strat 0°	6.52 ± 0.43	7.61 ± 0.28	4.26 ± 1.89	Non-significant	1.79 ± 0.01
Strat 67°	6.59 ± 0.29	7.42 ± 0.32	3.70 ± 0.26	Non-significant	0.64 ± 0.05

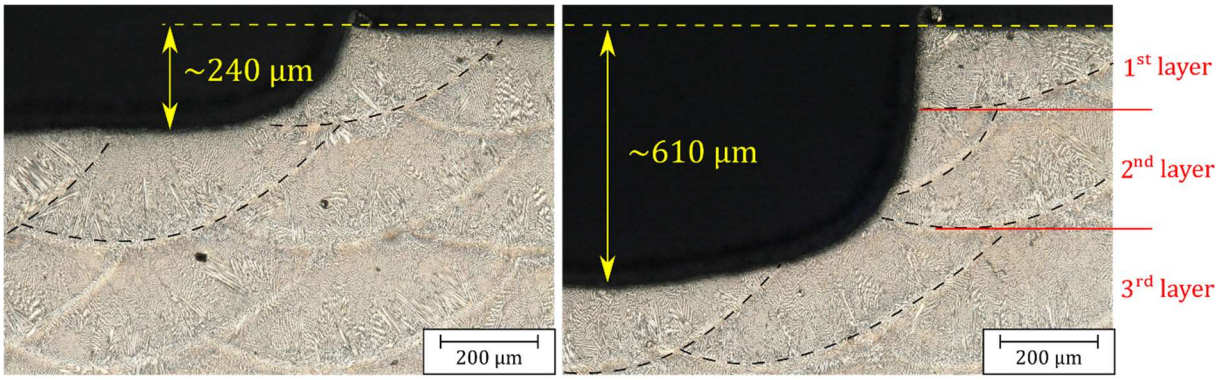

a) b)

Figure 15 : Wear tracks depth after a) 20 000 and b) 50 000 wear tests performed on the top surface of a coating manufactured with the strategy 0°. The black dashed lines highlight the beads.

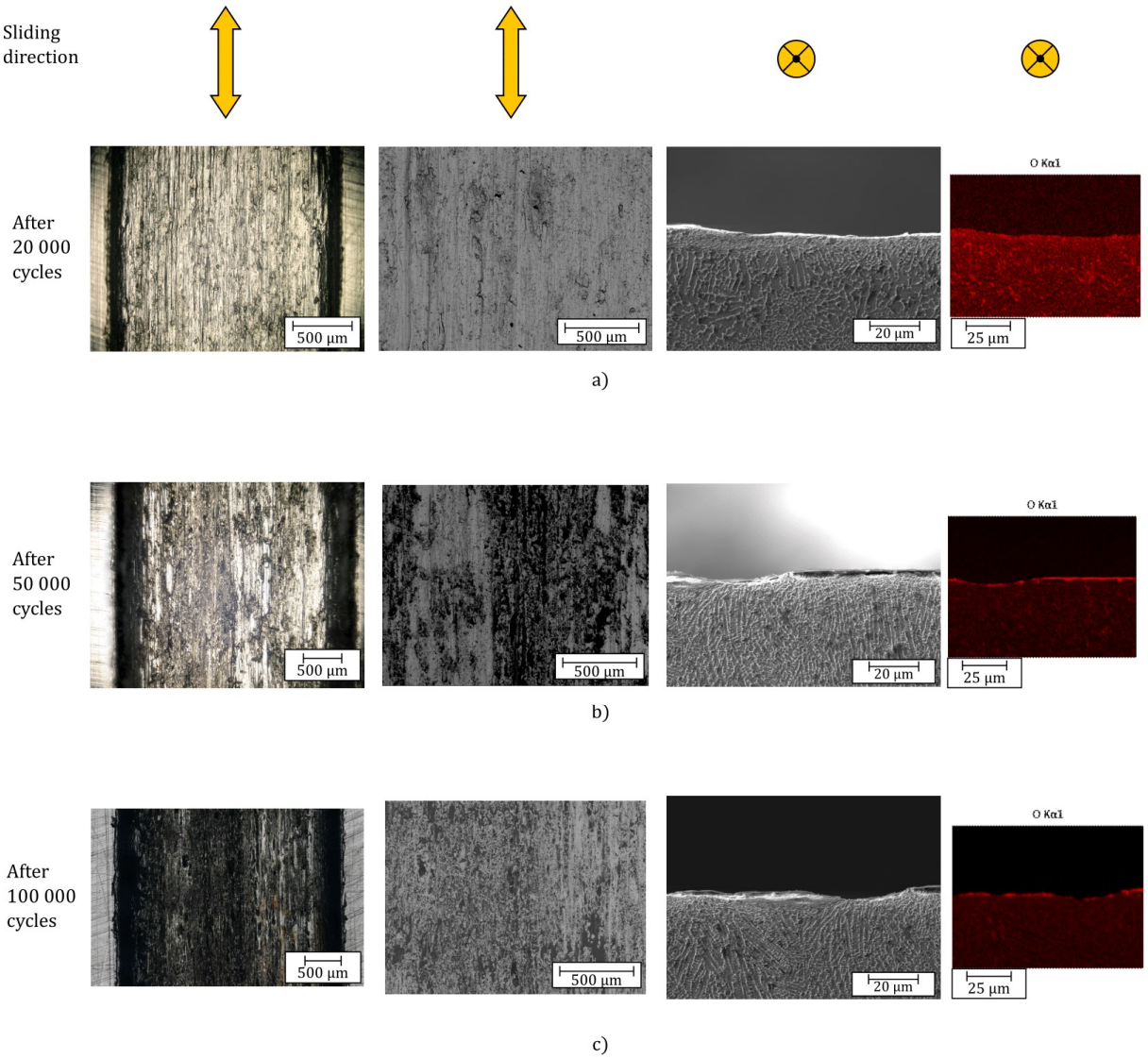

Figure 16: Optical images, SEM images of the top surface, SEM images of cross-section and its related EDS oxygen map of the surface of the LMD samples after they underwent wear test of a) 20 00; b) 50 000; c) 100 000 cycles respectively

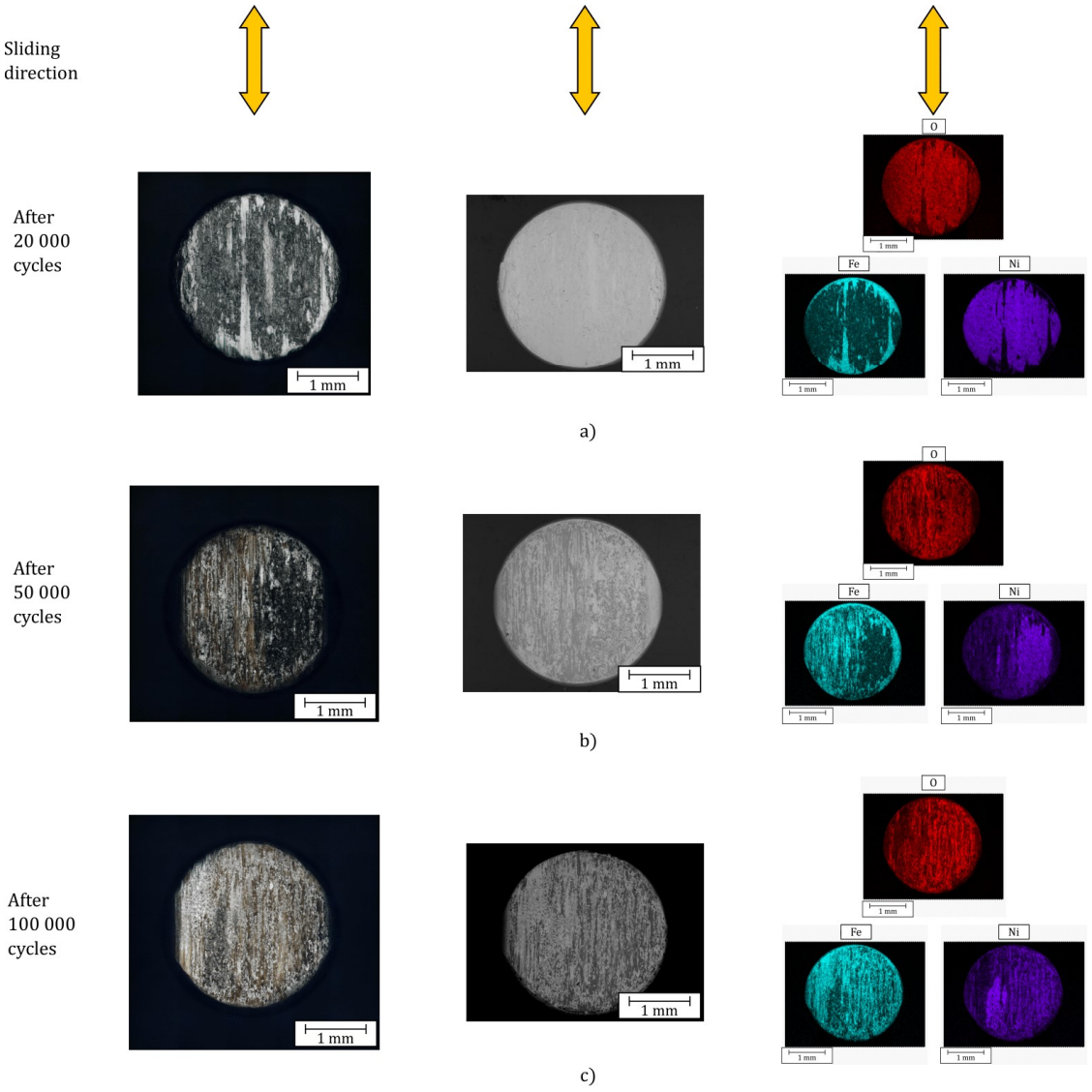

Figure 17: Optical images, SEM images and its related EDS oxygen, iron, and nickel maps of the pin obtained after a) 20 000; b) 50 000; c) 100 000 cycles respectively

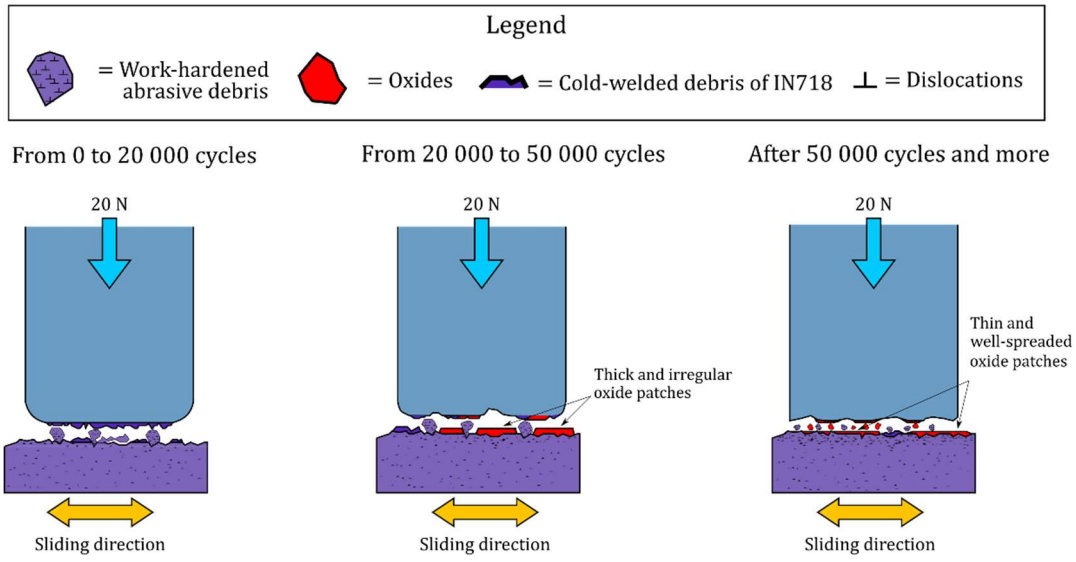

Figure 18: Evolution of the wear mechanisms with the number of cycles

3.3. Comparison of the wear behaviors of IN718 deposited by LMD and a conventionally manufactured IN718

The capability of a coating deposited by LMD to have at the very least the same wear resistance as the original piece is one of the criteria that defines a good wear-resistant coating. The wear resistance of the coated part by LMD is compared with a conventionally manufactured IN718. Interestingly, as exposed in Figure 19 a), the trend of the COF looks the same for both processes no matter the normal load used. It can be noted that, at 20 N, the COF is slightly lower when tests are performed on the wrought samples. However, a higher wear resistance of the wrought IN718 compared to the LMD samples is observed in Figure 19 b) and in Table 9. On average, LMD samples have a wear volume 14% larger than the wrought samples. As highlighted in Figure 20, because of the milling process, hardness variation is similar between both types of samples until 100 µm below the surface although the hardness of the samples built by LMD is slightly higher. As a consequence, hardness cannot explain the higher wear resistance of the wrought IN718. To identify the discrepancies in terms of wear mechanism at 20 N between both types of samples, the wear tracks were observed from different angles as displayed in Figure 21. From the top view, the wear tracks reveal different wear mechanisms depending on the processes used to process this alloy. The worn surface of the tests performed on the wrought alloy shows signs of strong plastic deformation (Figure 21 b)) with much less abrasion than for tests carried out on the LMD samples. From a transversal point of view, several layers are noticed. For the LMD sample (Figure 21 c) and e)), the first layer is composed of adhered IN718 debris. The presence of cracks below this layer testifies its easy delamination from the worn surface. Underneath, a highly plastically deformed region lies. The cellular sub-microstructure is no longer perceived and broken Laves phases are found. Then, further deep, the microstructure gets back to its classical cellular structure. For the conventional IN718, the transversal view reveals a thinner layer of adhered debris on the sliding surface. Some δ phases are found inside the adhered debris. The slip bands found inside the recrystallized grains is the proof of the plastic deformation induced by the dry wear test at the subsurface.

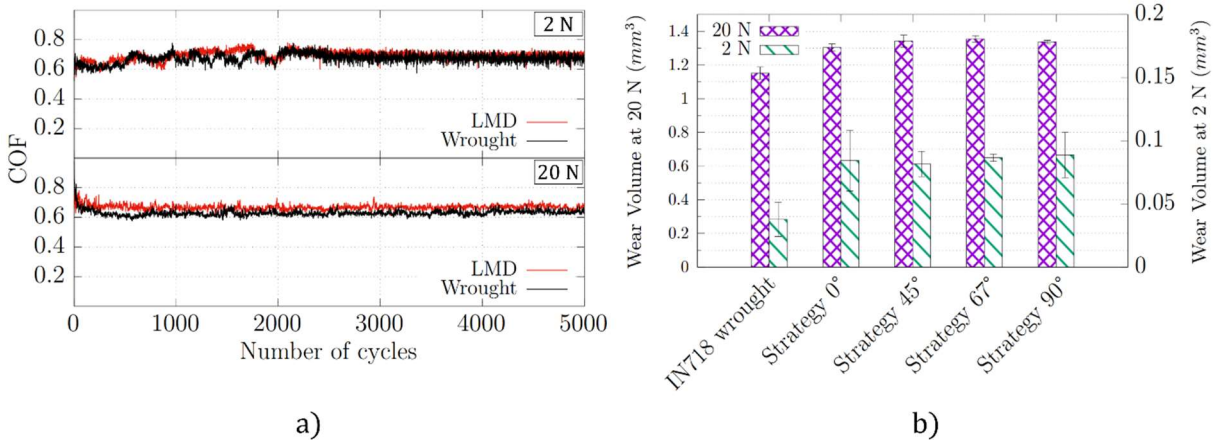

Figure 19 : a) Comparison of the evolution of the COF between the two processes for normal loads of 2 and 20 N; b) Wear volume comparison between wrought IN718 and the four different LMD samples

Table 9 : Wear rates according to the manufacturing process

Manufacturing process	Wear rates (*10^{-4} mm^3/Nm)
LMD	6.56 ± 0.25
Wrought	5.76 ± 0.02

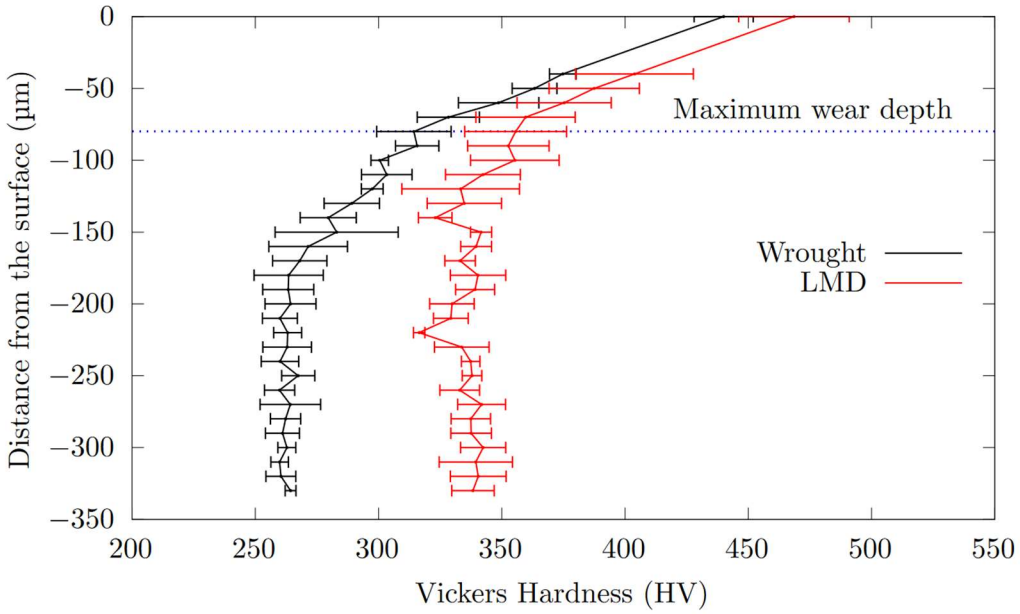

Figure 20: Hardness profile underneath the top milled surface (blue dotted lines shows the maximum depth reached after having performed a 20 N wear test for 5 000 cycles)

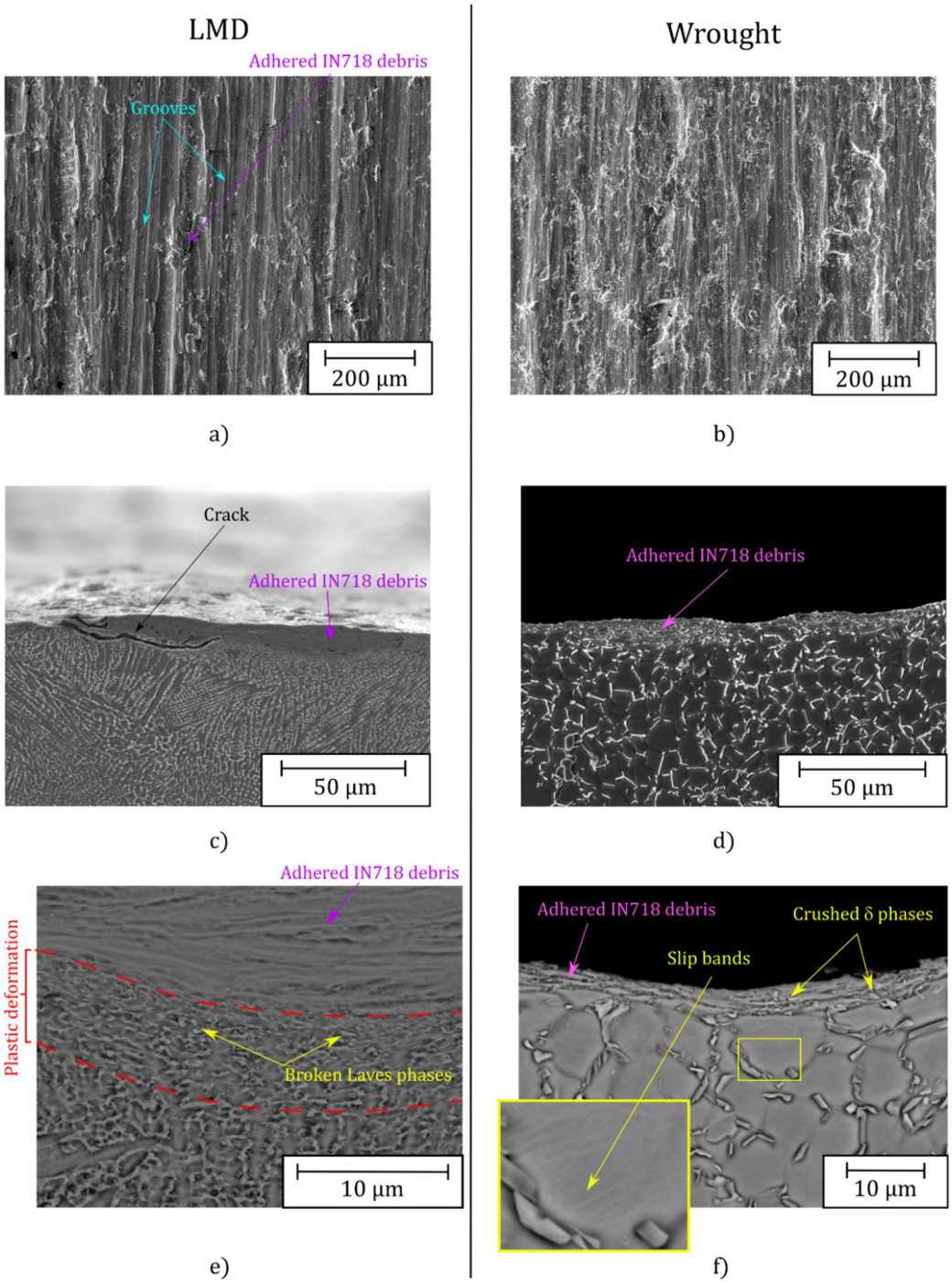

Figure 21 : SEM images of the wear tracks seen from different points of view (in the following order: top, side and zoomed side) of a,c,e) LMD and b,d,f) wrought samples (Test performed with: Fn = 20 N; f = 3 Hz; t = 5000 cycles)

Given the small hardness difference between both samples at the maximum wear depth shown in Figure 20, the wear volume discrepancies cannot be only justified through this material property. Such results might be explained through other aspects. One of them is the high amount of dislocations. The latter is caused by the deformation induced by the constrained thermal expansion and shrinkage of the material due to the LMD process. This leads to an initial amount of dislocations higher in the LMD as-built samples than in the wrought samples (subjected to successive heat treatments) [39]. As highlighted in Figure 22, in the unstrained regions far below the worn surface, the number of local defects with a misorientation around 1° is much greater in the LMD than the wrought. Those defects are directly linked to the high amount of dislocations trapped in the cell walls of the LMD sub-microstructure [40]. They might cause a hasty work-hardening of the LMD samples during the

wear test. The build-up of dislocations until a certain distance underneath the worn surface may bring about voids that would extend in cracks parallel to the surface. Once the crack reached the surface, delamination occurs [17]. In Figure 22 a), a deep strained region (~45 µm) is noticed which testifies that the piling up of defects near the sliding surface. Interestingly, no cracks were initiated from the porosity near the surface (~40 µm underneath the surface). However, the defects accumulated around it prove a deeper local deformation near this defect. Underneath the worn surface of the wrought sample, a thinner depth of defect accumulation is observed (~15 µm). This difference might be explained by the low amount of dislocations in its recrystallized microstructure compared to the LMD samples. Due to the initial difference in the amount of dislocations, the work-hardening rate is much higher for the LMD samples which promotes the early peeling off of the debris compared to the wrought samples. Moreover, the brittle Laves phases found in the LMD samples might have a detrimental effect on the wear resistance of the coatings. It has been proved by Sui et al. that, during fatigue and tensile tests, those phases promote the initiation of cracks [50][51]. δ phases found in the wrought microstructure, contrary to the Laves phases, are more prone to deform before dissolving and transforming into spherical phases [52].

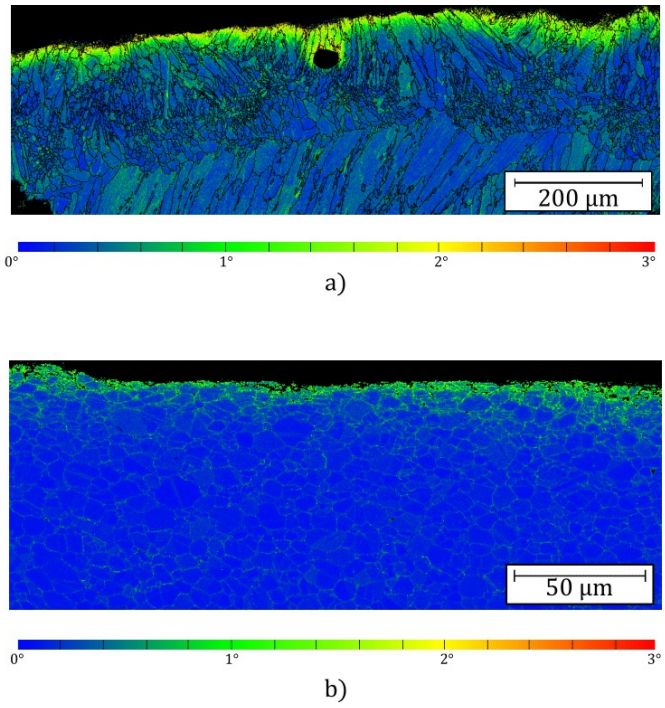

Figure 22: Kernel Average Misorientation (KAM) maps of the transversal views of the worn surface a) LMD and b) wrought samples which were subjected to a wear test with a 20 N normal load. Note: both maps have different scales.

As summarized in Figure 23, the lower wear resistance of the LMD samples is due to its brittle behavior caused by its high initial amount of dislocations, which brings forward its work hardening. Its brittleness could be also due to the Laves phases which promote cracks. Thus, its brittle behavior stimulates the generation of a high amount of debris which will accelerate wear by abrading the surface. At the early stage of the wear test, the wrought sample might behave similarly than LMD samples because of its highly strained microstructure caused by the milling. However, once the work-hardened layer is removed, its quasi-defect-free microstructure gives rise to more plastic deformation and thus limits the formation of potential abrasive debris.

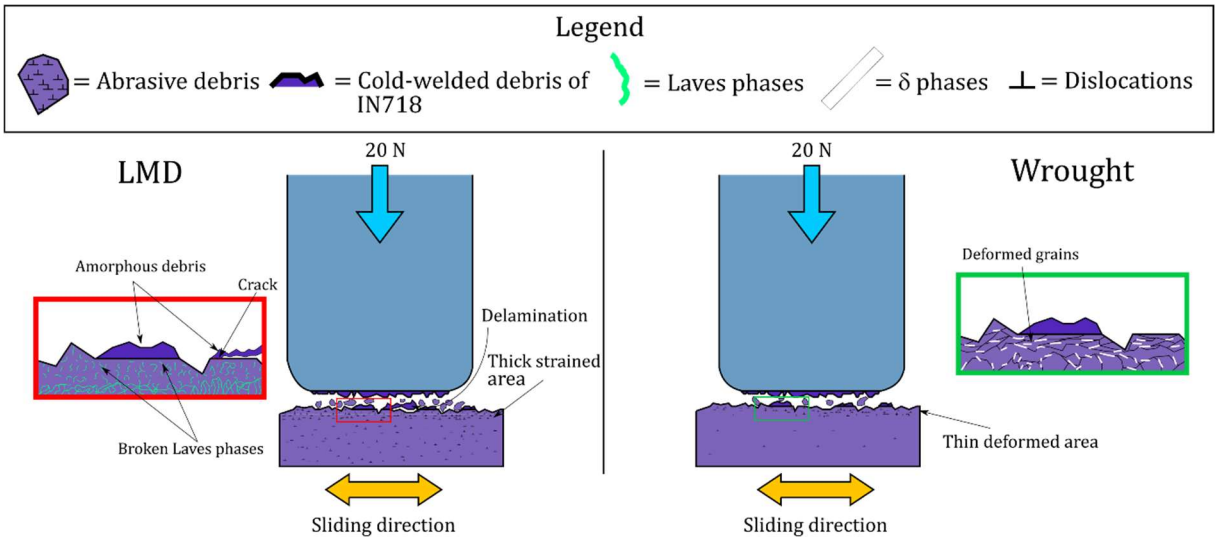

Figure 23 : Schematic describing the different wear mechanisms between the IN718 processed by LMD and wrought

4. Conclusion

This study sought to evaluate the wear resistance of IN718 coatings performed by LMD with different scanning strategies. In this aim, they were subjected to flat-on-flat reciprocating sliding wear tests. The wear behavior of the coated parts under several tribological conditions was studied, and a comparative investigation (in terms of wear volume, wear mechanisms and COF) with wrought IN718 was carried out. The following conclusions can be drawn:

- In the case of flat-on-flat contact, the scanning strategy used to deposit the coatings does not have a significant impact on the wear, despite the heterogeneous mechanical properties of the top surface

- The main wear mechanisms are abrasion and adhesion except for the 2 N load tests where a protective oxidized transfer layer remains in the contact. As the normal load increases, the abrasion becomes more evident than the adhesion. However, despite this slight change in wear mechanisms, the wear volume increases linearly with the applied load.

- As the number of cycles increases, the LMD samples wear in the same way no matter which strategies were employed. From 50 000 cycles, a protective layer composed of oxides prevents the coatings' wear to the detriment of the counter-body.

- LMD samples wear 14% more than the wrought samples even though the conventionally manufactured samples have a lower hardness. This result can certainly be explained by the more brittle behavior of the coated part caused by its high initial amount of defects and the existence of Laves phases which would promote cracking and consequently the formation of a significant quantity of abrasive debris.

Data Availability

The raw/processed data required to reproduce these findings cannot be shared at this time as the data also forms part of an ongoing study.

Competing of interest

The authors declare that they have no known competing financial interests or personal relationships that could have appeared to influence the work reported in this paper.

Acknowledgements

The authors want to thank the Société nationale des chemins de fer français (SNCF, France) and the Direction Générale de l'Armement (DGA, France) who fund those research.

References

[1] B. Dutta, “Directed energy deposition (DED) technology,” *Ref. Modul. Mater. Sci. Mater. Eng.*, pp. 1–19, 2020, doi: 10.1016/b978-0-12-819726-4.00035-1.

[2] T. A. Tejedor, R. Singh, and P. Pilidis, “Maintenance and repair of gas turbine components,” *Mod. Gas Turbine Syst. High Effic. Low Emiss. Fuel Flex. Power Gener.*, pp. 565–634, 2013, doi: 10.1533/9780857096067.3.565.

[3] N. Curry, N. Markocsan, L. Östergren, X. H. Li, and M. Dorfman, “Evaluation of the lifetime and thermal conductivity of dysprosia-stabilized thermal barrier coating systems,” *J. Therm. Spray Technol.*, vol. 22, no. 6, pp. 864–872, 2013, doi: 10.1007/s11666-013-9932-9.

[4] J. M. Wilson, C. Piya, Y. C. Shin, F. Zhao, and K. Ramani, “Remanufacturing of turbine blades by laser direct deposition with its energy and environmental impact analysis,” *J. Clean. Prod.*, vol. 80, pp. 170–178, 2014, doi: 10.1016/j.jclepro.2014.05.084.

[5] G. Bi and A. Gasser, “Restoration of nickel-base turbine blade knife-edges with controlled laser aided additive manufacturing,” *Phys. Procedia*, vol. 12, no. PART 1, pp. 402–409, 2011, doi: 10.1016/j.phpro.2011.03.051.

[6] T. Ünal-Saewe, L. Gahn, J. Kittel, A. Gasser, and J. H. Schleifenbaum, “Process development for tip repair of complex shaped turbine blades with IN718,” *Procedia Manuf.*, vol. 47, no. 2019, pp. 1050–1057, 2020, doi: 10.1016/j.promfg.2020.04.114.

[7] R. Devine, C. Cullen, J. Foster, M. Kulakov, C. MacFadden, and S. Fitzpatrick, “Remanufacture of Hot Forging Dies By LMD-p Using a Cobalt Based Hard-Facing Alloy,” *BHM Berg- und Hüttenmännische Monatshefte*, vol. 166, no. 5, pp. 243–249, 2021, doi: 10.1007/s00501-021-01108-z.

[8] J. Leunda, C. Soriano, C. Sanz, and V. G. Navas, “Laser cladding of vanadium-carbide tool steels for die repair,” *Phys. Procedia*, vol. 12, no. PART 1, pp. 345–352, 2011, doi: 10.1016/j.phpro.2011.03.044.

[9] Y. N. Aditya, T. Dharish Srichandra, M. Tak, and G. Padmanabham, “To study the laser cladding of ultra high strength AerMet-100 alloy powder on AISI-4340 steel for repair and refurbishment,” *Mater. Today Proc.*, no. xxxx, 2020, doi: 10.1016/j.matpr.2020.09.154.

[10] T. M. Pollock and S. Tin, “Nickel-based superalloys for advanced turbine engines: Chemistry, microstructure, and properties,” *J. Propuls. Power*, vol. 22, no. 2, pp. 361–374, 2006, doi: 10.2514/1.18239.

[11] Y. Xu, Y. Gong, P. Li, Y. Yang, and Y. Qi, “The effect of laser power on the microstructure and wear performance of IN718 superalloy fabricated by laser additive manufacturing,” *Int. J. Adv. Manuf. Technol.*, vol. 108, no. 7–8, pp. 2245–2254, 2020, doi: 10.1007/s00170-020-05172-6.

[12] M. Ma, Z. Wang, and X. Zeng, “Effect of energy input on microstructural evolution of direct laser fabricated IN718 alloy,” *Mater. Charact.*, vol. 106, pp. 420–427, Aug. 2015, doi: 10.1016/J.MATCHAR.2015.06.027.

[13] C. Zhong, A. Gasser, J. Kittel, J. Fu, Y. Ding, and R. Poprawe, “Microstructures and tensile properties of Inconel 718 formed by high deposition-rate laser metal deposition,” *J. Laser Appl.*, vol. 28, no. 2, p. 022010, 2016, doi: 10.2351/1.4943290.

[14] E. Hosseini and V. A. Popovich, “A review of mechanical properties of additively manufactured Inconel 718,” *Addit. Manuf.*, vol. 30, no. September, p. 100877, 2019, doi: 10.1016/j.addma.2019.100877.

[15] Y. Yang, Y. Zhu, M. M. Khonsari, and H. Yang, “Wear anisotropy of selective laser melted 316L stainless steel,” *Wear*, vol. 428–429, no. January, pp. 376–386, 2019, doi: 10.1016/j.wear.2019.04.001.

[16] Y. Yang, X. Li, M. M. Khonsari, Y. Zhu, and H. Yang, “On enhancing surface wear resistance via rotating grains during selective laser melting,” *Addit. Manuf.*, vol. 36, no. September, 2020, doi: 10.1016/j.addma.2020.101583.

[17] M. Bahshwan, C. W. Myant, T. Reddyhoff, and M. S. Pham, “The role of microstructure on wear mechanisms and anisotropy of additively manufactured 316L stainless steel in dry sliding,” *Mater. Des.*, vol. 196, p. 109076, 2020, doi: 10.1016/j.matdes.2020.109076.

[18] M. Bahshwan, M. Gee, J. Nunn, C. W. Myant, and T. Reddyhoff, “In situ observation of anisotropic tribological contact evolution in 316L steel formed by selective laser melting,” *Wear*, vol. 490–491, no. November 2021, p. 204193, 2022, doi: 10.1016/j.wear.2021.204193.

[19] B. Jose, N. L. Parthasarathi, N. Arivazhagan, A. D. M, and U. Borah, “Study of Dry Sliding Wear and Contact Mechanism of Inconel 718 At Study of Dry Sliding Wear and Contact Mechanism of Inconel 718 At High Temperature,” no. June, 2018.

[20] Z. Xu, Z. Huang, J. Zhang, X. Xu, P. Li, F. Su, and M. Zhu, “Tribological behaviors and microstructure evolution of Inconel 718 superalloy at mid-high temperature,” *J. Mater. Res. Technol.*, vol. 14, pp. 2174–2184, 2021, doi: 10.1016/j.jmrt.2021.07.102.

[21] L. Bai, S. Wang, G. Yi, Y. Shan, S. T. Pham, A. K. Tieu, Y. Li, and R. Wang, “Temperature-mediated tribological characteristics of 40CrNiMoA steel and Inconel 718 alloy during sliding against Si3N4 counterparts,” *Friction*, vol. 9, no. 5, pp. 1175–1197, 2021, doi: 10.1007/s40544-020-0455-3.

[22] A. Günen, “Properties and high temperature dry sliding wear behavior of boronized Inconel 718,” *Metall. Mater. Trans. A Phys. Metall. Mater. Sci.*, vol. 51, no. 2, pp. 927–939, 2020, doi: 10.1007/s11661-019-05577-3.

[23] Z. Zhao, H. Qu, P. Bai, J. Li, L. Wu, and P. Huo, “Friction and wear behaviour of Inconel 718 alloy fabricated by selective laser melting after heat treatments,” *Philos. Mag. Lett.*, vol. 98, no. 12, pp. 547–555, 2018, doi: 10.1080/09500839.2019.1597991.

[24] C. Samuel. S, M. Arivarasu, and T. R. Prabhu, “High temperature dry sliding wear behaviour of laser powder bed fused Inconel 718,” *Addit. Manuf.*, vol. 34, no. April, p. 101279, 2020, doi: 10.1016/j.addma.2020.101279.

[25] Y. Zhu, J. Zou, and H. Yang, “Wear performance of metal parts fabricated by selective laser melting: a literature review,” *J. Zhejiang Univ. Sci. A*, vol. 19, no. 2, pp. 95–110, 2018, doi: 10.1631/jzus.A1700328.

[26] B. Onuike and A. Bandyopadhyay, “Additive manufacturing in repair: Influence of processing parameters on properties of Inconel 718,” *Mater. Lett.*, vol. 252, pp. 256–259, 2019, doi: https://doi.org/10.1016/j.matlet.2019.05.114.

[27] X. Song, J. Lei, Z. Gu, and S. Zhou, “Boosting wear properties of Inconel718 superalloy by uniform dispersing graphene nanoplatelets through laser melting deposition,” *J. Alloys Compd.*, vol. 834, p. 155086, 2020, doi: 10.1016/j.jallcom.2020.155086.

[28] AddUp Company, “BeAM,” 2023. https://www.beam-machines.fr/.

[29] Oerlikon, “Oerlikon AM,” 2020. https://www.oerlikon.com/am/en/offerings/metal-powders/.

[30] Aubert&Duval, “PYRAD53NW’s technical sheet,” 2023.

https://www.aubertduval.com/fr/nuance/738/.

[31] Oxford Instruments, “Oxford Instruments.” https://www.oxinst.com/.

[32] Z. Roell, “Zwick Roell,” 2023. https://www.zwickroell.com/products/hardness-testing-machines/.

[33] W. C. Oliver and G. M. Pharr, “Measurement of hardness and elastic modulus by instrumented indentation: Advances in understanding and refinements to methodology,” *J. Mater. Res.*, vol. 19, no. 1, pp. 3–20, 2004, doi: 10.1557/jmr.2004.19.1.3.

[34] Buehler, “Buehler,” 2023. https://www.buehler.com/.

[35] T. Zurcher, V. Fridrici, and E. Charkaluk, “Surface microstructure of an IN718 3D coating manufactured by Laser Metal Deposition,” *Mater. Charact.*, p. 113054, 2023, doi: https://doi.org/10.1016/j.matchar.2023.113054.

[36] L. L. Parimi, G. A. Ravi, D. Clark, and M. M. Attallah, “Microstructural and texture development in direct laser fabricated IN718,” *Mater. Charact.*, vol. 89, pp. 102–111, 2014, doi: https://doi.org/10.1016/j.matchar.2013.12.012.

[37] P. Tao, H. Li, B. Huang, Q. Hu, S. Gong, and Q. Xu, “The crystal growth, intercellular spacing and microsegregation of selective laser melted Inconel 718 superalloy,” *Vacuum*, vol. 159, pp. 382–390, 2019, doi: https://doi.org/10.1016/j.vacuum.2018.10.074.

[38] J. F. Radavich, “The physical metallurgy of cast and wrought alloy 718,” *Superalloys*, pp. 229–240, 2004, doi: 10.7449/1989/superalloys_1989_229_240.

[39] K. M. Bertsch, G. Meric de Bellefon, B. Kuehl, and D. J. Thoma, “Origin of dislocation structures in an additively manufactured austenitic stainless steel 316L,” *Acta Mater.*, vol. 199, pp. 19–33, 2020, doi: 10.1016/j.actamat.2020.07.063.

[40] W. M. Tucho, P. Cuvillier, A. Sjolyst-Kverneland, and V. Hansen, “Microstructure and hardness studies of Inconel 718 manufactured by selective laser melting before and after solution heat treatment,” *Mater. Sci. Eng. A*, vol. 689, no. February, pp. 220–232, 2017, doi: 10.1016/j.msea.2017.02.062.

[41] J. Nguejio, F. Szmytka, S. Hallais, A. Tanguy, S. Nardone, and M. Godino Martinez, “Comparison of microstructure features and mechanical properties for additive manufactured and wrought nickel alloys 625,” *Mater. Sci. Eng. A*, vol. 764, no. Julyg, p. 138214, 2019, doi: 10.1016/j.msea.2019.138214.

[42] Bruker, “Bruker,” 2023. https://www.bruker.com/en/products-and-solutions/test-and-measurement/3d-optical-profilers.html.

[43] J. F. Archard and W. Hirst, “The wear of metals under unlubricated conditions,” *Proc. R. Soc. London. Ser. A. Math. Phys. Sci.*, vol. 236, no. 1206, pp. 397–410, Jan. 1956, doi: 10.1098/rspa.1956.0144.

[44] S. H. Riza, S. H. Masood, and C. Wen, “Wear behaviour of DMD-generated high-strength steels using multi-factor experiment design on a pin-on-disc apparatus,” *Int. J. Adv. Manuf. Technol.*, vol. 87, no. 1, pp. 461–477, 2016, doi: 10.1007/s00170-016-8505-8.

[45] V. Anandakrishnan, S. Sathish, D. Muthukannan, V. Dillibabu, and N. Balamuralikrishnan, “Dry sliding wear behavior of Inconel 718 additively manufactured by DMLS technique,” *Ind. Lubr. Tribol.*, vol. 72, no. 4, pp. 491–496, 2020, doi: 10.1108/ILT-08-2019-0322.

[46] R. Gras, *Tribologie: Principes et solutions industrielles*. L’Usine nouvelle, 2008.

[47] B. Onuike and A. Bandyopadhyay, “Additive manufacturing in repair: Influence of processing parameters on properties of Inconel 718,” *Mater. Lett.*, vol. 252, pp. 256–259, 2019, doi: https://doi.org/10.1016/j.matlet.2019.05.114.

[48] K. G. Thirugnanasambantham and S. Natarajan, “Mechanistic studies on degradation in sliding wear behavior of IN718 and Hastelloy X superalloys at 500 °c,” *Tribol. Int.*, vol. 101, pp. 324–330, 2016, doi: 10.1016/j.triboint.2016.04.016.

[49] Y. Balit, E. Charkaluk, and A. Constantinescu, “Digital image correlation for microstructural analysis of deformation pattern in additively manufactured 316L thin walls,” *Addit. Manuf.*, vol. 31, no. September 2019, p. 100862, 2020, doi: 10.1016/j.addma.2019.100862.

[50] S. Sui, J. Chen, E. Fan, H. Yang, X. Lin, and W. Huang, “The influence of Laves phases on the high-cycle fatigue behavior of laser additive manufactured Inconel 718,” *Mater. Sci. Eng. A*, vol. 695, no. March, pp. 6–13, 2017, doi: 10.1016/j.msea.2017.03.098.

[51] D. Zhang, Z. Feng, C. Wang, W. Wang, Z. Liu, and W. Niu, “Comparison of microstructures and mechanical properties of Inconel 718 alloy processed by selective laser melting and casting,” *Mater. Sci. Eng. A*, vol. 724, pp. 357–367, 2018, doi: https://doi.org/10.1016/j.msea.2018.03.073.

[52] H. Y. Zhang, S. H. Zhang, M. Cheng, and Z. X. Li, “Deformation characteristics of δ phase in the delta-processed Inconel 718 alloy,” *Mater. Charact.*, vol. 61, no. 1, pp. 49–53, 2010, doi: 10.1016/j.matchar.2009.10.003.